Seismic source spectral properties of crack-like and pulse-like modes of dynamic rupture

Yongfei Wang[1,2], Steven M. Day[1]

[1]Department of Geological Sciences, San Diego State University, San Diego, California, USA.
[2]Scripps Institution of Oceanography, University of California, San Diego, La Jolla, California, USA

Key Points:

- Corner frequency changes in crack-like and pulse-like models
- Stress drop estimate varies with source characteristics
- Double spectral decay slopes

Corresponding author: Yongfei Wang, yow004@ucsd.edu

Abstract

Earthquake source properties such as seismic moment and stress drop are routinely estimated from far-field body-wave amplitude spectra. Some quantitative but model-dependent relations have been established between seismic spectra and source parameters. However, large variability is seen in the parameter estimates, and it is uncertain how the variability is partitioned among real variability in the source parameters, observational error and modeling error due to complexity of earthquake behaviors. Earthquake models with dynamic weakening have been found to exhibit two different modes of rupture: expanding crack and self-healing pulse modes. Four representative models are generated to model the transition from crack-like to pulse-like. Pulse-like rupture leads to development of a second corner frequency and the intermediate spectral slope is approximately 2 in most cases. The focal-sphere-averaged lower P and S wave corner frequencies are systematically higher for pulse-like models than crack models of comparable rupture velocity. The slip-weighted stress drop $\Delta\sigma_E$ exceeds the moment-based stress drop $\Delta\sigma_M$ for pulse-like ruptures, with the ratio ranging from about 1.3 to 1.65, while they are equal for the crack-like case. The variations in rupture mode introduce variability of the order of a factor of two in standard (i.e., crack-model based) spectral estimates of stress drop. The transition from arresting- to growing-pulse rupture is accompanied by a large (factor of ~1.6) increase in the radiation ratio. Thus, variations in rupture mode may account for the portion of the scatter in observational spectral estimates of source parameters.

1 Introduction

Estimates of earthquake source parameters such as seismic moment and rupture area are important to our understanding the physics of source processes and provide important input for the quantification of seismic hazards. These parameters are routinely measured from far-field seismic spectra. Low-frequency spectral level, corner frequency and the high-frequency spectral decay slope are related to seismic moment, rupture area and high-frequency energy radiation, respectively. Static stress drop, the difference between the average shear stress on the rupture surface before and after faulting, provides insights into surrounding tectonic environments where earthquakes are generated [e.g. *Kanamori and Anderson*, 1975; *Allmann and Shearer*, 2007, 2009]. Observational studies for worldwide mb 5.5 earthquakes give stress drop estimates in the range of 0.3 to 50 MPa and, despite the large scatter, the mean value is at most weakly dependent on magnitude [*Allmann and Shearer*, 2009]. In engineering applications, stress drop is recognized as an important parameter that scales high-frequency ground motion [e.g. *Hanks and McGuire*, 1981; *Boore*, 1983]. Moreover, the apparent magnitude independence of stress drops provides potential physical constraints on the magnitude dependence of empirically-based ground motion prediction equations (GMPEs) [*Baltay and Hanks*, 2014].

Stress drop may be estimated from measurements of coseismic slip and rupture area [*Eshelby*, 1957]. For earthquakes without extensive surface rupture, those quantities are not accessible to direct measurement, and (apart from relatively large events with extensive geodetic observations) they must be inferred from the spectral content of far-field P and S waves. The seismic moment and source dimension, estimated from low-frequency limit and corner frequency f_c of seismic spectra, respectively, are then used to derive stress drop estimates. Variability in determinations of stress drop arises not only from uncertainties and biases in observational data selection and processing, but also from the source model assumptions used [e.g. *Savage*, 1966; *Brune*, 1970; *Sato and Hirasawa*, 1973; *Molnar et al.*, 1973; *Dahlen*, 1974; *Madariaga*, 1976; *Kaneko and Shearer*, 2014, 2015] and the methodology used in fitting the spectra to the model spectral shape [*Shearer et al.*, 2006]. Moreover, there is no agreement among investigators on which types of theoretical models should be used for estimating the source dimensions, and what degree of model simplification is appropriate [*Kaneko and Shearer*, 2014].

The analytical solution for the elliptical uniform stress drop crack model in a homogeneous Poissonian medium with major and minor axes A and B [*Eshelby*, 1957; *Madariaga*, 1977a] gives a relationship between moment, area and stress drop,

$$\Delta\sigma = \frac{M_0}{c_1 SB}, \tag{1}$$

where M_0 is the seismic moment, S is the source area and c_1 is a geometric parameter. For slip along the major axis, c_1 is defined as:

$$c_1 = \frac{4}{3E(m) + [E(m) - \frac{B^2}{A^2}K(m)]/m^2}, \tag{2}$$

where $m = \sqrt{1 - B^2/A^2}$ and $K(m)$ and $E(m)$ are complete elliptical integrals of the first and second kinds, respectively [*Eshelby*, 1957; *Madariaga*, 1977a]. In the special case of a circular source ($R = A = B$), the relationship (Eq-1) simplifies to

$$\Delta\sigma = \frac{7M_0}{16R^3}, \tag{3}$$

where R is the rupture radius. Given a theoretical model of the source parameterized by the single length scale R, the source radius can be inferred from the focal-sphere average of corner frequency $\overline{f_c}$ of the P or S wave through [*Brune*, 1970; *Madariaga*, 1976]

$$\overline{f_c} = k\frac{\beta}{R}, \tag{4}$$

where β is the shear wave speed and k is a constant that is model dependent. Hence, estimates of stress drop can be computed as combinations of the expressions above:

$$\Delta\sigma = \frac{7}{16}(\frac{\overline{f_c}}{k\beta})^3 M_0. \tag{5}$$

Among these variables involved in stress drop determination under the assumption of a circular crack, only the value of k depends on which theoretical relationship is used to associate corner frequency with source radius. Both f_c and k (but not their ratio) depend on wavetype, which we will indicate with superscripts. The model proposed by *Brune* [1970] presumes a simple circular fault and obtained $k^S = 0.37$, a value which is frequently used for inferring source dimension and stress drop [e.g. *Hanks and Thatcher*, 1972; *Archuleta et al.*, 1982; *Baltay et al.*, 2011]. An alternative is the source model of *Sato and Hirasawa* [1973], which includes nucleation, constant-velocity spreading and instantaneous stopping of circular rupture. This model is established by presuming the *Eshelby* [1957] static solution; given rupture velocity $V_r = 0.9\beta$, the model gives $k^P = 0.42$ and $k^S = 0.29$. Although this model is consistent with a known static solution [*Eshelby*, 1957] and explicitly incorporates propagation and stopping of the rupture front followed by slip cessation, and is favored by many investigators [e.g. *Prejean and Ellsworth*, 2001; *Stork and Ito*, 2004; *Imanishi and Ellsworth*, 2013], a defect is that slip ceases at the same instant everywhere over the fault plane. Accordingly, some refinements have been proposed; for example, *Molnar et al.* [1973] make modifications such that slip at a point starts with the arrival of the rupture front and continues until information from the edges of the fault is radiated back to the point. *Dahlen* [1974] extended the analysis of rupture kinematics to an elliptical crack that keeps on growing with the same shape.

The model of *Madariaga* [1976] has been widely accepted and used [e.g. *Abercrombie*, 1995; *Prieto et al.*, 2004; *Shearer et al.*, 2006; *Allmann and Shearer*, 2007, 2009; **?**]. *Madariaga* [1976] simulated a dynamic singular crack model with constant rupture velocity using a staggered-grid finite-difference method and found that $k^P = 0.32$ for P wave and $k^S = 0.21$ for S wave for $V_r = 0.9\beta$. *Kaneko and Shearer* [2014] constructed a dynamic model of expanding rupture on a circular fault with cohesive zone that prevents a stress singularity at the rupture front. Their solutions (obtained with a spectral element method) give $k^P = 0.38$ and $k^S = 0.26$ for the same rupture speed. Moreover, *Kaneko and Shearer* [2015] extended their analysis to symmetric and asymmetric circular and elliptical models with subshear and supershear ruptures.

Previous studies using dynamic theoretical source models [e.g. *Madariaga*, 1976; *Kaneko and Shearer*, 2014, 2015] for quantifying relationship between seismic spectra and stress drop are all based on so-called crack-like rupture models, i.e., those in which the duration of slip at a point on the fault is comparable to the overall duration of rupture. They have also been limited to source models with constant rupture velocity and prescribed rupture termination edges. An alternative rupture mode, the so-called pulse-like rupture, has not been considered in the development of dynamic model-based spectral theories (though the purely kinematic model of *Haskell* [1964] is pulse-like). Pulse-like rupture, in which slip duration at a representative point (i.e., slip risetime) is short relative to the rupture duration, may occur when dynamic weakening occurs during the most rapid sliding phase and is followed by restrengthening. Pulse-like rupture can also result from the presence of secondary length scales (e.g., in the fault geometry, frictional parameter distribution, or stress field) shorter than the overall rupture dimension. Short slip risetimes inferred from kinematic source inversions were first interpreted as evidence of a local healing mechanism by *Heaton* [1990]. This mechanism has also been introduced to explain the complexity of seismicity patterns [*Cochard and Madariaga*, 1996] and the lack of heat flow anomaly on the San Andreas Fault [*Noda et al.*, 2009]. Theoretical self-similar solution for pulse-like rupture has been derived by [*Nielsen and Madariaga*, 2003]. Both crack- and pulse-like modes have been observed in laboratory experiments and numerical simulations [e.g. *Lu et al.*, 2010; *Zheng and Rice*, 1998]. The mechanisms behind the pulse-like rupture modes that have been proposed include: the velocity dependent friction [*Heaton*, 1990; *Beeler and Tullis*, 1996; *Zheng and Rice*, 1998; *Gabriel et al.*, 2012], coupling between slip and dynamic normal stress changes along bimaterial faults [*Andrews and Ben-Zion*, 1997; *Ampuero and Ben-Zion*, 2008; *Dalguer and Day*, 2009], the spatial heterogeneity of fault strength and initial shear stress [*Beroza and Mikumo*, 1996; *Day et al.*, 1998; *Oglesby and Day*, 2002], the finite downdip width of the seismogenic zone [*Day*, 1982; *Johnson*, 1992] or the reflected waves within the fault zone [*Huang and Ampuero*, 2011].

Here we simulate 4 simplified models of rupture propagating and (in one case) stopping spontaneously in expanding crack and self-healing pulse-like modes. The spontaneous rupture model, described in Section 2, incorporates strong velocity weakening in a regularized rate- and state-dependent friction framework [*Noda et al.*, 2009; *Rojas et al.*, 2009]. Section 3 gives a qualitative description of the simulation results. Computation of far-field radiated spectra is described in Section 4, and spectral parameters are discussed in Sections 5 and 6. Section 7 discusses retrieval of energy and stress drop estimates.

2 Crack-like and pulse-like modes generation with forced or spontaneous termination

Among multiple mechanisms already mentioned for the generation of self-healing rupture, here we focus on velocity dependent friction. The rate and state framework on which we base the friction law we use in this paper has its basis in laboratory experiments [e.g. *Dieterich*, 1979; *Ruina*, 1983; *Marone*, 1998]. We use the regularized formulation of the friction coefficient f as proposed by *Lapusta et al.* [2000] (see also *Shi and Day* [2013], Appendix B),

$$f(V,\psi) = a\sinh^{-1}[\frac{V}{2V_0}\exp(\frac{\psi}{a})], \tag{6}$$

where the state variable ψ evolves according to a slip law

$$\dot{\psi} = -\frac{V}{L}[\psi - \psi_{ss}(V)], \tag{7}$$

$$\psi_{ss}(V) = a\ln\{\frac{2V_0}{V}\sinh[\frac{f_{ss}(V)}{a}]\}, \quad (8)$$

where V is slip velocity and $f_{ss}(V)$ is the steady-state friction coefficient at slip velocity V. In this study, the steady-state friction coefficient takes the form (following *Dunham et al.* [2011] and *Shi and Day* [2013], which is a smoothed version of the form used by *Noda et al.* [2009] and *Rojas et al.* [2009])

$$f_{ss}(V) = f_w + \frac{f_{lv} - f_w}{[1 + (V/V_w)^8]^{1/8}}, \quad (9)$$

which has a strongly velocity-weakening feature such that when $V \gg V_w$, f_{ss} approaches a fully weakened friction coefficient f_w. V_w is called weakening slip velocity. When $V << V_w$, f_{ss} approaches a low-velocity steady-state friction coefficient f_{lv}, i.e.,

$$f_{lv}(V) = f_0 - (b - a)\ln(V/V_0). \quad (10)$$

In the foregoing equations, the constants a and b are the direct-effect and state-evolution parameters, respectively, and f_0 and V_0 are the reference values for the friction coefficient and slip rate, respectively.

One commonly-applied way to generate a transition from crack-like to pulse-like rupture mode is to alter the background shear stress level [e.g. *Cochard and Madariaga*, 1996; *Perrin et al.*, 1995; *Beeler and Tullis*, 1996; *Zheng and Rice*, 1998; *Noda et al.*, 2009; *Dunham et al.*, 2011; *Gabriel et al.*, 2012]. Figure 1, based on the analysis of *Zheng and Rice* [1998] shows this schematically. The transition from pulse-like to crack-like rupture mode is controlled by the relative values of the initial shear stress τ^b and a critical stress value τ_{pulse}, where the latter, as defined by *Zheng and Rice* [1998], is equal to the zero-velocity intercept of the radiation damping line (blue dashed line) tangent to the steady-state weakening curve (red solid curve). The rupture mode can be changed from pulse-like to crack-like by varying the initial shear stress from below to above a fixed τ_{pulse}. For convenience in comparing stress drop, we apply here an alternative scheme that maintains initial stress state and instead varies the weakening slip rate V_w. As Figure 1 shows, this variation can also generate a transition between crack-like and pulse-like modes as it shifts the steady-state velocity-weakening curve towards the right, thus shifting τ_{pulse} from below to above a fixed initial shear stress.

We examine rupture of a planar surface embedded in an infinite homogeneous Poissonian medium (Figure 2), with velocity weakening friction (i.e., $a < b$) operating on the interior of a circle of radius R, with velocity strengthening ($b < a$) on the exterior (as a device to limit the rupture extent, with the ratio of $(b - a)/a$ exceeding 10, an essentially unbreakable barrier). The material properties and initial stress state are given in Table 1. For convenience of comparison among multiple simulation scenarios, the initial stress state is held fixed, as are the frictional parameters, apart from the weakening slip velocity V_w. Variations of the latter parameter are used to generate the transition from crack-like to pulse-like rupture. Rupture is initiated by imposing a shear stress perturbation $\Delta\tau^0(x_1, x_2)$ at the center of prescribed circular region (yellow circle in Figure 2), which elevates the initial shear stress to $\tau^b(x_1, x_2) + \Delta\tau^0(x_1, x_2)$. $\Delta\tau^0(x_1, x_2)$ has the following expression:

$$\Delta\tau^0(x_1, x_2) = c\exp(\frac{l^2}{l^2 - R_n^2})H(R_n - l)\tau^b(x_1, x_2), \quad (11)$$

where c is coefficient representing over-stress amplitude, l is the distance between fault point (x_1, x_2) and hypocenter (x_1^h, x_2^h), $l = \sqrt{(x_1 - x_1^h)^2 + (x_2 - x_2^h)^2}$, R_n is the nucleation region radius, H is the Heaviside step function and $\tau^b(x_1, x_2)$ is the uniform equilibrium initial shear stress on the fault. The chosen shape function in Eq-11 is smooth (infinitely differentiable and of compact support) in order to prevent singular behavior at the edge of the nucleation zone. The amplitude of the shear stress perturbation and the size of nucleation may affect the rupture mode, and we have chosen values that, in combination with

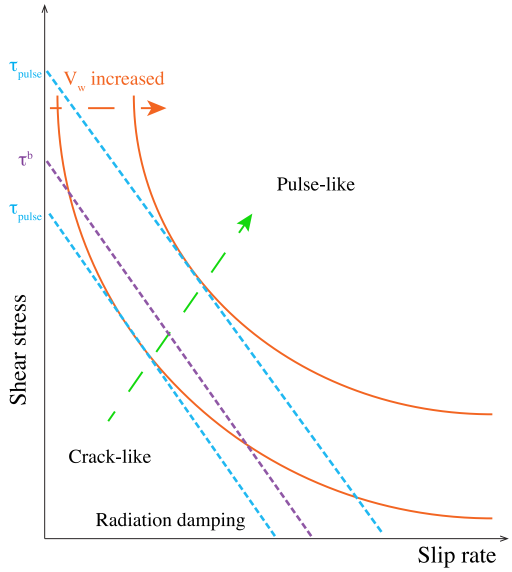

Figure 1. Schematic illustration indicating how the weakening slip rate V_w generates the rupture mode transition between crack-like and pulse-like. The red solid lines denote steady-state shear stress dependent on slip rate. Blue and purple dashed lines are radiation damping lines corresponding to different V_w values. For the small value of V_w, the corresponding critical τ_{pulse} is below initial background shear stress and a crack-like rupture mode is obtained. With V_w increased such that τ_{pulse} is elevated above the initial shear stress, based on the analysis in *Zheng and Rice* [1998], the rupture mode becomes pulse-like.

the chosen range of frictional parameters and background shear stress, permit rupture in either crack-like or pulse-like mode. We examine the slip rate and stress evolution along two perpendicular profiles through the hypocenter, an inplane profile (aligned with the initial shear stress) and an antiplane profile (perpendicular to initial shear stress). In addition to admitting pulse-like ruptures, the study further differs from related numerical studies of seismic spectra [*Madariaga*, 1976; *Kaneko and Shearer*, 2014, 2015], in that it is based on a spontaneous rupture model rather than a fixed rupture-velocity model. Rupture velocity is determined as part of the problem solution, and may fluctuate in response to, e.g., local background stress state, fault geometry and frictional conditions.

Accurate numerical results require adequate resolution of the cohesive zone, i.e., the portion of the fault surface (at a given instant of time) which is slipping at an appreciable rate but has not yet fully weakened. Based upon rough estimates [e.g. *Shi and Day*, 2013; *Dunham et al.*, 2011] and detailed measurements [e.g. *Rojas et al.*, 2009] of the size of cohesive zone, we expect a cohesive zone dimension averaging 500m or so, and we formulate the numerical simulations to ensure at least 20 nodes within the cohesive zone. Based on this level of resolution, the benchmark solutions in simulations done using slip weakening and rate- and state-based friction laws investigated by *Day et al.* [2005] and *Rojas et al.* [2009], respectively, all indicated relative rms errors for peak slip rate are much below 10 percent, with one to two orders of magnitude smaller error for their other metrics (e.g., mean static slip and rupture velocity).

We solve 3-D problem of rupture in a viscoelastic medium using SORD (Support Operator Rupture Dynamics) [*Ely et al.*, 2008, 2009]. This code uses a generalized finite difference method with spatial and temporal second-order accuracy. The frictional

Table 1. Models Parameter Values

Parameter	Symbol	Value
	Bulk Properties	
Compressive wave speed	V_P	6000 m/s
Density	ρ	2670 kg/m^3
Poisson's ratio	ν	0.25
	Frictional Parameters	
Direct effect parameter	a	0.01
Evolution effect parameter	b	0.014
Reference slip velocity	V_0	1 μm/s
Steady-state friction coefficient at V_0	f_0	0.7
State-evolution distance	L	0.4 m
Weakening slip velocity	V_w	variable
Fully weakened friction coefficient	f_w	0.2
	Initial Conditions	
Normal stress on fault	σ^0	120 MPa
Background shear stress	τ^b	38 MPa
Initial slip velocity	V_{ini}	2×10^{-9}m/s
Prescribed rupture radius	R	18 km
	Nucleation Parameters	
Nucleation radius	R_n	3000 m
Overstress	$\Delta\tau^0$	$1 \times \tau^b$

equations 6 through 10 are solved using the staggered velocity-state method of *Rojas et al.* [2009]. The full methodology has been verified in tens of benchmark scenarios developed by the Southern California Earthquake Center [*Harris et al.*, 2009] and this code has been used in numerous studies of spontaneous dynamic rupture simulation and strong ground motion [e.g. *Ely et al.*, 2010; *Ben-Zion et al.*, 2012; *Shi and Day*, 2013; *Song et al.*, 2013; *Baumann and Dalguer*, 2014; *Song*, 2015; *Vyas et al.*, 2016].

3 Numerical simulation results

In this section, we present simulation results representing a range of rupture modes from crack-like to pulse-like, as obtained by adjusting the weakening slip velocity V_w (letting it range from 0.05 m/s to 0.1 m/s). We examine four examples, including an expanding crack case and three pulse-like cases. The latter are denoted growing, steady-state, and arresting pulse models, following commonly-used terminology, [e.g. *Noda et al.*, 2009; *Gabriel et al.*, 2012]. These names reflect the spatial pattern of slip, as seen in Figure 3, which shows some details of the slip distributions for these cases. Figures 3a and 3b show the slip distribution at equal time intervals (1s), for profiles on the inplane (Mode II) and antiplane (Mode III) axes, respectively. For the expanding crack case, slip amplitude is strongly dependent on the distance to hypocenter, whereas all three pulse-like ruptures show more nearly uniform slip distributions. The mechanism for generating pulse-like rupture is that hypothesized by *Heaton* [1990], and can be seen from the shear stress spatial and temporal evolution near the crack tip in Figure 3c and 3d. In the expanding crack example, shear stress remains almost constant following full weakening, whereas, in pulse-like ruptures, the shear stress increases in response to slip-rate reduction behind the rupture front, eventually healing the rupture and creating a pulse-like slip rate function.

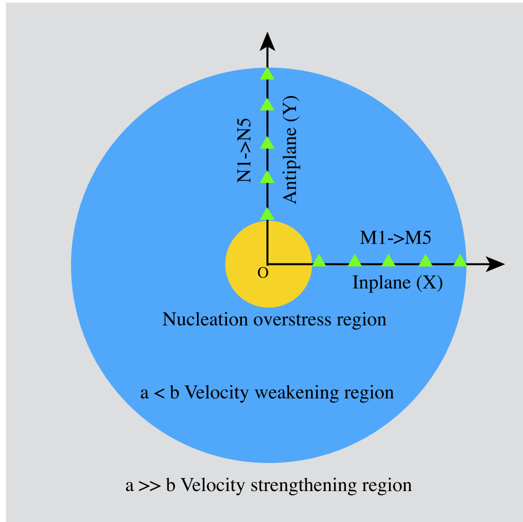

Figure 2. Circular fault model for generating the transition between crack-like and pulse-like ruptures. The yellow circle in the center is the nucleation area with overstress. The blue circular patch is velocity weakening region where $a < b$ and rupture is allowable. Outer grey region requires $a >> b$, velocity strengthening, to arrest rupture. X and Y axis correspond to inplane and antiplane direction along which the green triangular symbols are receivers used to record slip rate function in Figure 3-7.

Further details of the crack-like rupture example are shown are Figure 4. The characteristic decrease of slip amplitude from the center toward the unbreakable barrier is evident in Figure 4a. This shape is, however, not identical with the standard elliptical slip distribution (as a function of radial distance) for a purely static crack, because there is some degree of variability of the static stress change (Figure 4b) with slightly larger static stress drop along the anti-plane direction and at the edges, due to the barrier as well as the directional dependence of rupture velocity that is shown in Figure 4c. The slip rate function, shown in Figure 4d and 4e, has the familiar long-tailed shape, terminated by stopping phases from the rupture edge, and shows the characteristic increase in peak slip rate with the distance away from the hypocenter.

Details of the growing pulse example are shown in Figure 5. Due to the self-healing behavior, the slip distribution in this case (Figure 5a, with corresponding stress changes in Figure 5b) is more uniform than in the expanding crack model, but there are high-slip lobes along anti-plane direction, near the rupture edge. These two high slip lobes are the result of the differing rupture velocities along the two axes indicated in Figure 5c. Also seen in Figures 5a is a large slip patch associated with the artificial nucleation at the center of the fault. The principal difference relative to the expanding-crack model is in the shape of the slip rate function, shown in Figures 5d and 5e. The slip rate takes the form of a pulse with nearly constant rise time (weakly dependent upon distance). Stopping phases are no longer evident at the stations close to boundary. However, the slip rate function in this case still retains the feature of the expanding crack model that peak slip rate increases from center to edge. This feature has a significant effect (to be discussed later) on far-field wave shapes for the growing pulse case.

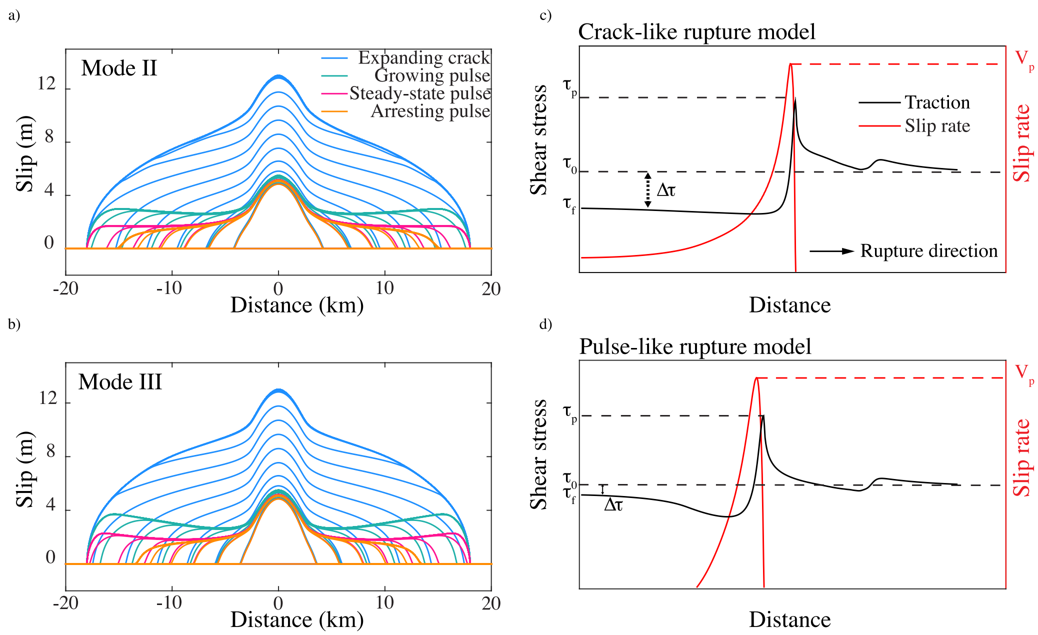

Figure 3. Numerical simulation results of 4 rupture models: expanding crack (blue), growing pulse (green), steady-state pulse (pink) and arresting pulse (orange). (a) and (b) show time dependent slip (1s interval) along inplane and antiplane direction, and the characteristic slip profiles of the respective rupture modes are observed. The dependence of slip on the distance from the hypocenter is minimal in pulse-like mode, but (apart from the nucleation zone) has the expected elliptical shape in the crack-like case. (c) and (d) show shear stress (black line) and slip rate (red line) for crack-like and pulse-like ruptures. In the pulse-like mode (d), shear stress has a re-strengthening phase that heals the rupture and reduces the slip duration, in contrast to the flat residual shear stress and longer slip duration in the crack-like rupture (c).

Most features of the steady-state pulse model are similar to those of the growing pulse, but slip is more uniformly distributed and smaller on average, while mean stress drop and rupture velocity are both decreased (Figure 6a, 6b and 6c). The slip rate function is again pulse shaped, but with reduced rise time compared with the growing-pulse case, and now the peak slip rate is almost invariant with the distance to edges (Figure 6d and 6e). The duration of the slip rate function is also almost invariant with distance, as in the growing pulse model. That is, the rupture front velocity is close to the healing front velocity (outside the nucleation zone), and this is consistent with simulated results of *Gabriel et al.* [2012].

The arresting pulse case (Figure 7) corresponds to a weakening slip velocity that is close to the maximum value that permits a rupture to escape the nucleation area, and results in a rupture model that stops spontaneously, i.e., before reaching the imposed velocity-strengthening barrier. In Figure 7d and 7e, peak slip rate decays to zero as hypocentral distance increases. This feature of spontaneous arrest distinguishes this case from the other three models. It is also a departure from previous rupture models used in the study of the far-field spectrum, all of which involve arrest by edge barriers, with the result that the high-frequency spectral character in those previous models is dominated by stopping phases.

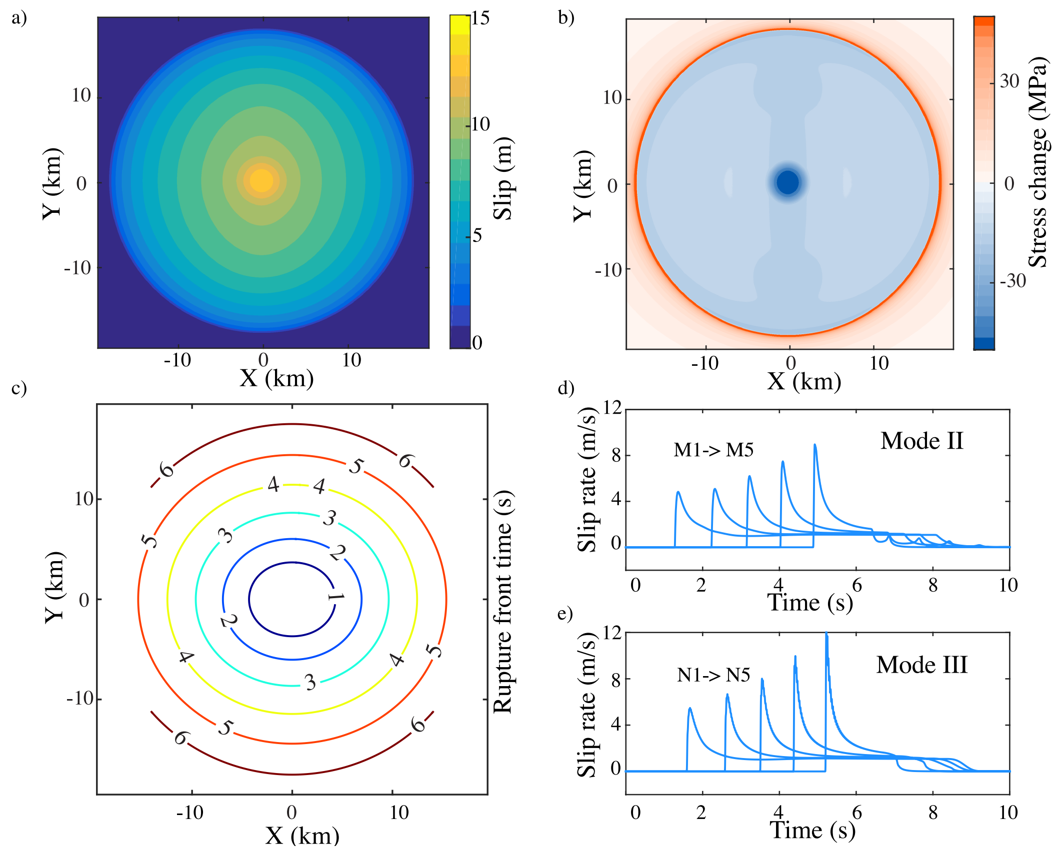

Figure 4. Details of expanding crack, showing slip (a), static stress change (blue region means stress drop) (b), rupture front time (c) and slip rate functions (d) and (e).

4 Computation of far-field radiations and spectra

Our analysis of the simulations focuses on the far-field body-wave spectra from these sources, calculated for an elastic wholespace, following *Madariaga* [1976]; *Kaneko and Shearer* [2014, 2015]. We use the representation theorem of *Aki and Richards* [2002] to compute far-field P and S wave displacements at $\vec{x}$ as:

$$
\begin{aligned}
u_i(\vec{x},t) \quad &= \quad \frac{\gamma_i}{4\pi\rho\alpha^3 r_0} C_{jkpq}\gamma_p\gamma_q\nu_k n_j \iint \Delta\dot{u}(\vec{\xi}, t-\frac{r}{\alpha})dS \\
&\quad + \frac{\delta_{ip}-\gamma_i\gamma_p}{4\pi\rho\beta^3 r_0} C_{jkpq}\gamma_q\nu_k n_j \iint \Delta\dot{u}(\vec{\xi}, t-\frac{r}{\beta})dS \\
&\quad (i,j,k,p,q=1,2,3),
\end{aligned}
\tag{12}
$$

where ρ is the density, α and β are P and S wave speed, r_0 is the distance from a reference point on fault to the receiver, C_{jkpq} is the elastic modulus, γ_q is the unit vector directed from source point to the receiver point, ν_k is the unit vector normal to fault surface, n_j is the direction of slip vector, $\vec{\xi}$ is a point on fault and r is the distance between $\vec{\xi}$ and $\vec{x}$ (eq. 10.6 of [*Aki and Richards*, 2002]). Here, we use the fact that the fault surface is flat, neglect variations of the slip direction about its average, and employ the approximation that the receiver distance is large compared with the source dimension (and r_0 can be taken as the mean value of r, with the understanding that $|r-r_0| \ll r$).

The far-field amplitude spectra are obtained by taking the amplitude of the Fourier transform of the far-field P and S displacements, respectively. As is customary in obser-

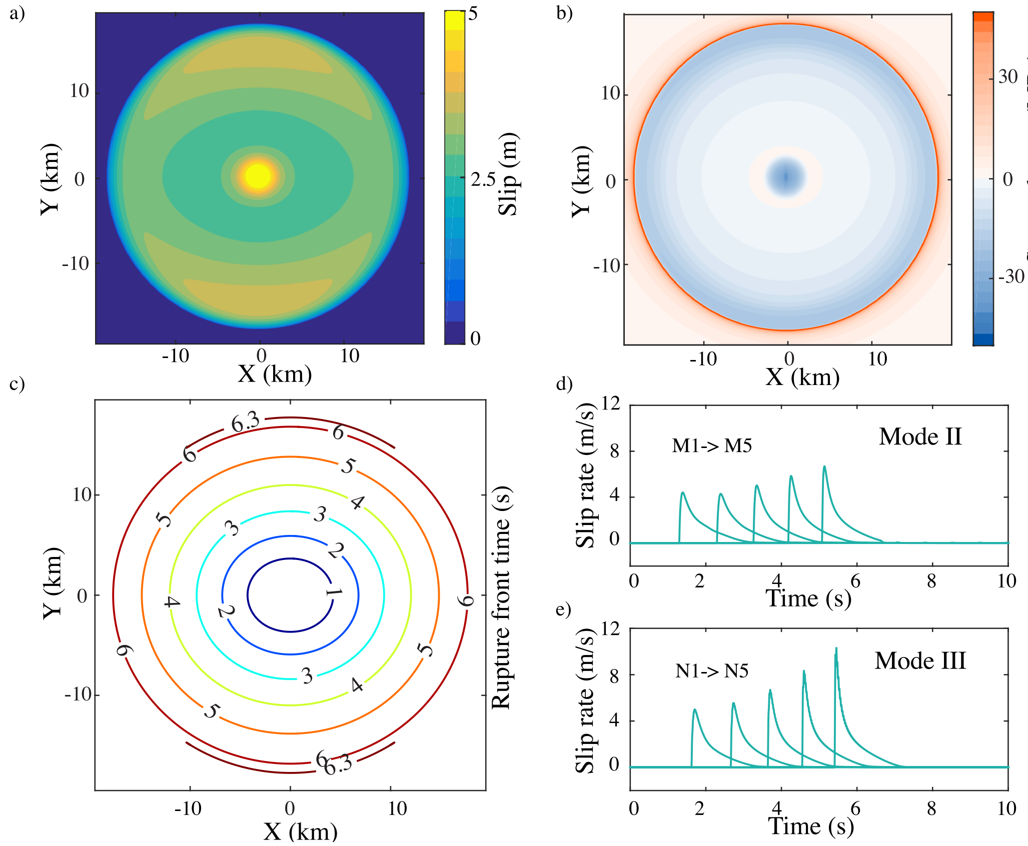

Figure 5. Details of growing pulse, showing slip (a), static stress change (b), rupture front time (c) and slip rate functions (d) and (e).

vational studies, we introduce a specific spectral model and use least-square fitting to estimate the model parameters. The Brune type spectral model (generalized for arbitrary high-frequency asymptotic slope) is used here,

$$U(f) = \frac{\Omega_0}{1 + (f/f_c)^n}, \tag{13}$$

where Ω_0 is the long period spectral level proportional to the seismic moment, f_c is the corner frequency and n is the spectral fall-off rate. We estimate the spectral parameters Ω_0, f_c and n for the simulated far-field spectra by using a grid search to minimize their misfit to the Brune model spectrum in the frequency band of $0.05 f_c < f < 20 f_c$. In calculating the misfit, a weight function is used to balance the contributions of different frequency components by roughly equalizing contributions from equal increments of log(f), a procedure with precedent in observational studies [*Prieto et al.*, 2004; *Shearer et al.*, 2006].

5 Detailed analysis of properties of far-field displacements and spectra

In this section, we present for each source model, the far-field displacements, the corresponding spectra, and the consequent spherical distribution of the corner frequencies and fall-off rates obtained from the spectral fitting. We begin by summarizing the variation of the spectral corner frequency and fall-off rate over the focal sphere, interpreting them in terms of the rupture characteristics identified in Section 3. For that purpose, we select 8 receivers with different take-off angle (defined as the angle between the vector

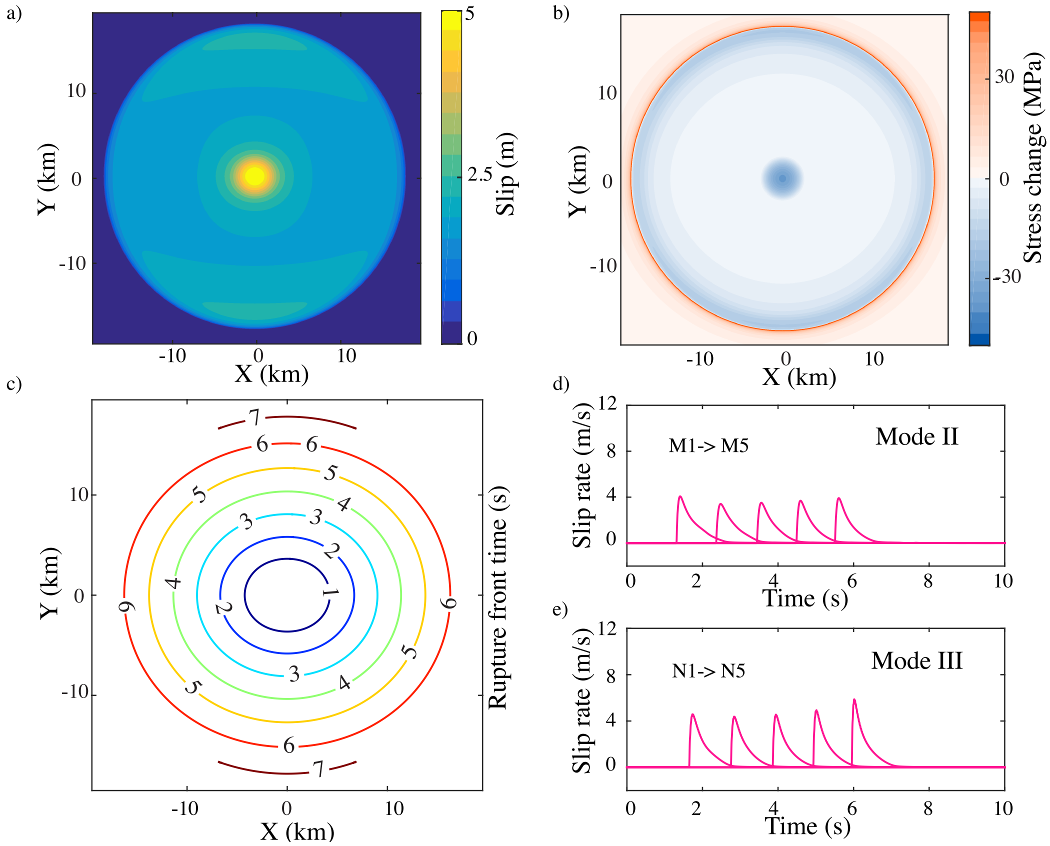

Figure 6. Details of steady-state pulse, slip (a), static stress change (b), rupture front time (c) and slip rate functions (d) and (e).

normal to the fault and the vector pointing to the receiver from the source), and fixed azimuthal angle (22.5 degrees to the x axis). Their displacements and spectra, with stars representing computed corner frequencies, are plotted in Figure 8. The models representing the four different rupture modes can be distinguished by the four colors (and this color convention for the four rupture modes is followed throughout the paper).

In discussing the far-field displacements, it is common to refer to their time-domain form as "displacement pulses." These radiated pulses are not to be confused with the pulses of fault-surface slip velocity that characterizes the pulse-like rupture models. Similarly, we follow convention and use "rise time" in this section to refer to the time between the onset and peak of the far-field displacement, which is not to be confused with our (also conventional) use of the same term to refer to the duration of the slip pulses in the pulse-like rupture models.

Several factors affecting the far-field displacement pulses and corresponding spectral shapes in Figure 8 should be noted. In these multilateral ruptures, the pulse rise times (duration between onset and peak value of displacement pulse) are shorter in directions at low angle to the fault plane (high take-off angle) than they are in directions nearly normal to the fault. The rise time is controlled by both the focusing due to directivity and increasing peak slip rate in the direction of rupture propagation [*Brune et al.*, 1979]. The overall pulse width is longer at high take-off angle, which is a (well-known) rupture directivity effect. The pulse width is heavily influenced by stopping phases generated from the edges [*Madariaga*, 1976]. In the case where rupture velocity is constant and stopping occurs

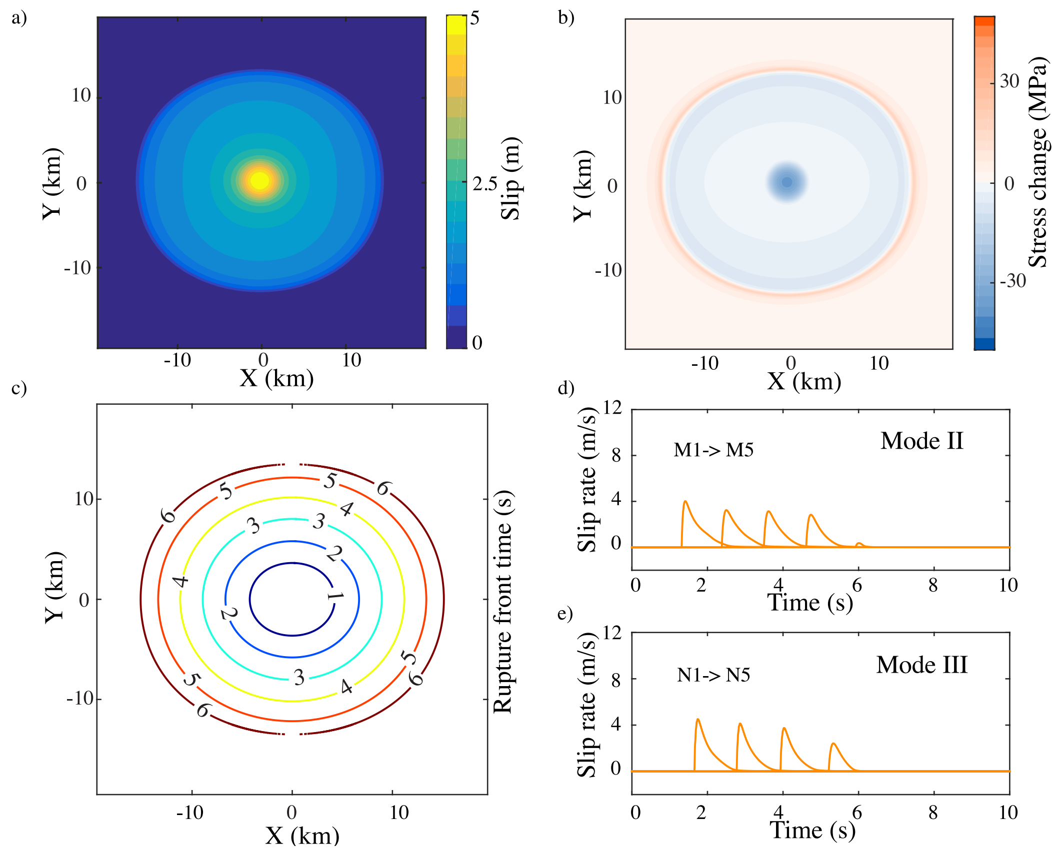

Figure 7. Details of arresting pulse, showing slip (a), static stress change (b), rupture front time (c) and slip rate functions (d) and (e).

on a circular boundary, delay times of the stopping phases from the nearest and farthest points on the edge of the fault would be

$$t = R(\frac{1}{V_R} \mp \frac{\sin\theta}{c}), \tag{14}$$

where R means fault size, V_R is rupture velocity, c is wave speed, θ is take-off angle, minus sign denotes the nearest, and positive sign denotes the farthest, stopping phases. In Figure 8, the peak value of displacement is usually controlled by the nearest stopping phase and the approximate pulse width is controlled by the farthest stopping phase, but the pattern is complicated by rupture velocity changes and variations in the rupture mode and slip-velocity distribution. Nucleation phases are common to all models (i.e., the four curves overlap during first few tenths of a unit of dimensionless time), since they result from a common rupture-initiation procedure.

As the take-off angle is increased, the rise time is shortened while the overall duration is lengthened, as suggested by Eq-14. These two factors have opposing influences on high- to low-frequency spectral ratios, with the result that the trend of corner frequency with takeoff angle is non-monotonic, especially for the crack-like model, consistent with the studies of *Madariaga* [1976] and *Kaneko and Shearer* [2014]. Compared with the crack-like rupture mode, the pulse-like ruptures have P and S waveforms with sharper peaks, in the case of growing and steady-state pulse models, and smoother shapes, in the arresting pulse case (due to disappearance of the stopping phase). These effects generate more complex behavior of the seismic spectra, reflected in the variations in spherically-average values of corner frequency and fall-off rate among 4 models shown in Table 2.

Table 2. Spectral parameters of P and S waves among 4 models [a]

	Expanding crack	Growing pulse	Steady-state pulse	Arresting pulse
V_r^2	0.88β	0.85β	0.78β	0.72β
V_r^3	0.84β	0.81β	0.74β	0.66β
k^P	0.35	0.40	0.31	0.28
k^S	0.27	0.36	0.31	0.34
$\frac{k^P}{k^S}$	1.3	1.1	1.0	0.8
n^P	2.2	2.0	1.8	1.7
n^S	1.9	1.9	1.8	1.9
k^P_{stack}	0.38	0.43	0.31	0.28
k^S_{stack}	0.30	0.39	0.31	0.31
$\frac{k^P_{stack}}{k^S_{stack}}$	1.3	1.1	1.0	0.9
n^P_{stack}	2.2	2.0	1.8	1.8
n^S_{stack}	2.0	1.8	1.8	1.9

[a] V_r^2 and V_r^3 denote rupture velocity along inplane and antiplane direction. k^P and k^S are normalized corner frequencies, $f_c\beta/R$, for the P and S wave, respectively. n^P and n^S are (absolute values of) the spectral slopes for the P and S wave, respectively. Unsubscripted quantities are obtained by averaging separate spectral estimates obtained from each receiver direction. Subscript "stack" indicates that the quantity is an estimate obtained from an amplitude spectrum ("stack") formed by averaging the individual amplitude spectra from all receiver directions.

The rupture velocities given in Table 2, V_r^2 and V_r^3, are along the X (inplane motion) and Y (antiplane motion) coordinate axes, respectively. Each is computed by a linear integral $\int V_r dl/L$ along the ruptured portion of the coordinate axis, excluding the nucleation zone. In this equation, V_r is the local rupture velocity, l is the distance variable, and L is the rupture length excluding the nucleation zone.

In the remainder of this section, we elaborate on the features of far-field displacement pulses, their corresponding spectral amplitudes, and the spatial distributions (on the focal sphere) of the spectral parameters, for the four representative rupture models described in Section 3, illustrated in Figures 9-12.

Figure 9 shows results for the expanding crack model. Figures 9a and 9b show the spherical distributions (calculated at 5 degree intervals) of normalized corner frequency (corner frequency divided by the ratio of source radius to S velocity) and spectral fall-off rate, while 9c shows the far-field body wave displacement pulses and 9d shows their spectra. We use the same notation as *Madariaga* [1976], *Kaneko and Shearer* [2014] and

Kaneko and Shearer [2015]. Near the fault surface (equator or low latitudes in Figure 9), the resultant corner frequencies are generally smaller than average, as a result of the wider displacement pulse width, as indicated in Figure 9c. The variation of pulse width is due to source directivity and duration, which reflects the differential traveling time between the near and far side of fault termination signals (Eq-14). In addition, spectral fall-off rates are generally larger at higher latitudes stations. There are, in addition, some complexities in the corner-frequency and fall-off rate distributions that arise from dynamic effects not present in previous, fixed rupture velocity models. For example, four lobes of high fall-off rate at high latitude (i.e., at take-off angle near fault normal), result from the dissimilar rupture behaviors along the in-plane and anti-plane directions typical in spontaneous rupture models (though corner frequencies do not show a corresponding strong azimuthal dependence). We obtain the following spherically averaged corner frequencies and fall-off rates for P and S waves,

$$\begin{aligned}\overline{f_c^P} &= k^P\frac{\beta}{R} = 0.35\frac{\beta}{R}\\ \overline{f_c^S} &= k^S\frac{\beta}{R} = 0.27\frac{\beta}{R}.\end{aligned}\tag{15}$$

The k values are sometimes called normalized corner frequency and for the convenience of comparing results with previous studies and other scenarios here, we use normalized corner frequency, instead of original corner frequency. Rupture velocities average 0.88β along inplane and 0.84β along antiplane direction, respectively. Spherically averaged spectral fall-off rates for P and S waves, termed as n^P and n^S, are 2.2 and 1.9, respectively. The values of k^P and k^S found here are very close to results of symmetrical circular rupture with fixed rupture speed of 0.8β in *Kaneko and Shearer* [2014]. This is because for our spontaneously propagating expanding crack model, the far-field pulse width is mainly dominated by anti-plane rupture, which has the lower rupture velocity. Slight differences with *Kaneko and Shearer* [2014] in the distributions of corner frequencies and spectral fall-off rates is attributable to spontaneity of ruptures, effects of the rupture-initiation method and frequency band used in spectral fitting.

Figure 10 shows the results for the growing pulse model. The variation of waveform pulse width with take-off angle seen in the expanding crack model is still apparent, while the azimuthal dependency is slightly reduced. Relative to the expanding crack case, the growing-pulse corner frequencies are higher and spectral decaying slopes are steeper (Figure 10a and 10b), as can be inferred from the narrower far-field displacement pulse width (Figure 10c). The estimated rupture velocities of 0.85β along inplane and 0.81β along antiplane direction are not appreciably (less than 4%) different from the expanding crack case. The spherically averaged corner frequencies for the growing pulse case are

$$\begin{aligned}\overline{f_c^P} &= k^P\frac{\beta}{R} = 0.40\frac{\beta}{R}\\ \overline{f_c^S} &= k^S\frac{\beta}{R} = 0.36\frac{\beta}{R},\end{aligned}\tag{16}$$

and spherically averaged n^P and n^S are 2.0 and 1.9, respectively. The normalized P and S corner frequencies are increased by about 14% and 33%, respectively, relative to the expanding crack. This corner frequency shift and the reduced spectral fall-off rates result from the shorter slip duration in the growing pulse model. The P to S corner frequency ratio (~1.1) is lower for the growing pulse rupture than for crack-like models (~1.3 in our spontaneous crack model and ~1.35 in the crack model of *Kaneko and Shearer* [2014] with similar rupture velocity).

Figure 11 shows results for the steady-state pulse model. In this case, in addition to the effect of take-off angle, there are also slight azimuthal variations (Figure 11a). Nucleation phases (sharp onset of wave pulses) are larger relative to the overall pulse amplitude than in the crack and growing-pulse models. Spectral decay slopes are lower compared with the growing crack and growing pulse models, and there is an accompanying downward shift in corner frequency. Somewhat smaller rupture velocities (0.78β along inplane and 0.74β along antiplane) also contribute to the reduction of corner frequencies. The spherically averaged corner frequencies for the steady-state pulse case are

$$\begin{aligned}\overline{f_c^P} &= k^P \frac{\beta}{R} = 0.31 \frac{\beta}{R} \\ \overline{f_c^S} &= k^S \frac{\beta}{R} = 0.31 \frac{\beta}{R},\end{aligned} \tag{17}$$

and spherically averaged fall-off rates for P and S waves are 1.8 and 1.8, respectively. The ratio between P and S wave corner frequencies is ∼1.0, a reduction relative to the previously discussed cases, consistent with previous studies showing near-equality of P and S corner frequencies for complex sources (e.g., the asymmetrical circular model of *Kaneko and Shearer* [2015]).

Figure 12 shows results for the arresting pulse model. This is the only case in which rupture growth stops spontaneously, without encountering the circular barrier. The absence of distinct stopping phases introduces some significant differences compared with the previous models. The most prominent difference is the smoothing of the peak of the radiated waveforms (Figure 12c), which were sharply cusped in the other models. In addition, for the arresting-pulse case the initiation phase is relatively large compared to the overall amplitude of the radiated waveform. The normalized corner frequency for P waves (Figure 12a) has a pattern similar to that of the other cases, with somewhat lower values for receivers at focal-sphere equatorial receivers (at high angle to the fault normal) relative to near-polar receivers (low angle to the fault normal). But for S waves, that pattern is reversed, with corner frequencies lower near the fault normal. Moreover, the fall-off rates of S waves near the focal equator are much larger than those at other locations. Average rupture velocities for the arresting-pulse rupture (0.72β along inplane and 0.66β along antiplane) are somewhat lower than for the previous cases. The spherically averaged corner frequencies for the arresting pulse model are

$$\begin{aligned}\overline{f_c^P} &= k^P \frac{\beta}{\sqrt{AB}} = 0.28 \frac{\beta}{\sqrt{AB}} \\ \overline{f_c^S} &= k^S \frac{\beta}{\sqrt{AB}} = 0.34 \frac{\beta}{\sqrt{AB}},\end{aligned} \tag{18}$$

where A and B are major and minor axes of elliptical slip distribution in Figure 7a. The spherically averaged n^P and n^S are 1.7 and 1.9, respectively. The high-frequency asymptotic slope reflects the lowest-order singularity present in a waveform, so it might seem paradoxical that the n values (especially n^P) are reduced in this case, given that the waveform cusps have been smoothed. The reason is that we (deliberately) calculate n values using a frequency band appropriate to observational studies (as explained in Section 4). In the presence of the complexities introduced by pulse-like rupture, the resulting n values actually characterize an intermediate spectral slope, not the ultimate high-frequency asymptote. This issue is discussed in detail in the next section. The P corner frequency is slightly (∼10%) larger than for the corresponding fixed rupture-velocity crack-model estimate [*Kaneko and Shearer*, 2014], while the S corner frequency is ∼30% larger. In fact, the arresting-pulse model has a P to S corner frequency ratio of ∼0.82, the only one of our cases in which the ratio is less than one. This apparently anomalous behavior is partly a consequence of the high spectral fall-off rate for S at low latitudes of the focal sphere. The higher spectral slope at the low latitudes has the effect of shifting the corner frequency to higher frequencies, even though the high-frequency spectral energy is actually diminished in the arresting-pulse model relative to the other models. The P wave corner frequency, in contrast, decreases relative to the steady-pulse model, roughly by the amount expected due to the decreased rupture velocity (following *Kaneko and Shearer* [2014]).

These results are compared with those of previous studies [*Brune*, 1970; *Sato and Hirasawa*, 1973; *Madariaga*, 1976; *Kaneko and Shearer*, 2014], all of which were limited to crack-like modes with fixed rupture velocity. As shown in Table 3, the spherical average corner frequencies of pulse-like modes shows dependency on rupture velocity, which is also observed in previous models [*Sato and Hirasawa*, 1973; *Kaneko and Shearer*, 2014], though rupture velocity has less impact on the S corner frequency than on the P corner. Both P and S wave corner frequencies are affected by rupture mode transition from crack-like to pulse-like. Results in Table 2 also indicate that rupture mode only minimally affects the spectral fall-off rate estimates; apart from the arresting pulse case, these slope estimates are near 2, consistent with other studies [*Brune*, 1970; *Madariaga*, 1976; *Kaneko and Shearer*, 2014]. The P wave spectral slope estimate for the arresting pulse case is lower, around 1.7. We emphasize that all spectral slope estimates were made using the procedure and bandwidth described in Section 4, which is intended to be consistent with observational practice. As shown in the next section, the estimates for the pulse-like models actually represent intermediate spectral trends, not asymptotic slopes.

6 Properties of stacked spectra

In the previous section, the average corner frequency estimate $\overline{f_c}$ is an average of corner frequency of each spectrum weighted by spherical subarea (following the methodology of *Madariaga* [1976], *Kaneko and Shearer* [2014] and *Kaneko and Shearer* [2015]). On the other hand, observational studies [e.g. *Prieto et al.*, 2004; *Shearer et al.*, 2006] frequently use an alternative corner frequency estimate, $\overline{f_c}$, derived directly from spectral stacks. That approach may provide a more robust estimation, since it reduces effects of spectral distortion due to source and propagation complexities. To investigate the effects of our rupture models on source parameter estimates, we recalculate the average corner frequencies of P and S waves by stacking the logarithms of all individual spectra of each wave type, evenly sampling the focal sphere. In Table 2, the values of k^P_{stack}, k^S_{stack}, n^P_{stack} and n^S_{stack} derived from stacked spectra are compared with those estimated by averaging individual spectral parameters in the previous section. The mean differences between the two averages (considering all four rupture models together) are 4%, 8%, 1% and 3% for k^P, k^S, n^P and n^S, respectively, confirming that observational estimates of source parameters are only minimally affected by performing the parameter estimation on the spectral stack.

Stacked spectra for the four models are shown in Figure 13, along with Brune spectra fit to them by the method described in Section 4. The spectra in Figure 13 are only shown for frequencies well below the high-frequency resolution limit of the numerical simulations. In the expanding crack model, the Brune spectral function represents the stacked spectra of P and S waves with negligible misfit (Figures 13b and 13c, respectively). This is also consistent with previous studies [*Madariaga*, 1976; *Kaneko and Shearer*, 2014, 2015]. The three pulse-like models, however, have systematic misfits at high frequency. The mismatch takes the form of a secondary corner frequency that becomes progressively better developed as the rupture mode progresses from growing to arresting pulse behavior.

Table 3. Spectral parameters compared with previous studies.[a]

Model name	V_r^2/β	V_r^3/β	k^P	k^S	k^P_{KS}	k^S_{KS}	k^P_{Ma}	k^S_{Ma}	k^P_{SH}	k^S_{SH}	k^S_B
Brune's model	Infinite	Infinite									0.37
$KS - Ma - SH$ models	0.9	0.9			0.38	0.26	0.32	0.21	0.42	0.29	
⋆ **Expanding crack**	0.88	0.84	0.35	0.27							
⋆ **Growing pulse**	0.85	0.81	0.40	0.36							
$KS - SH$ models	0.8	0.8			0.35	0.26			0.39	0.28	
⋆ **Steady-state pulse**	0.78	0.74	0.31	0.31							
$KS - SH$ models	0.7	0.7			0.32	0.26			0.36	0.27	
⋆ **Arresting pulse**	0.72	0.66	0.28	0.34							
$KS - SH$ models	0.6	0.6			0.30	0.25			0.34	0.27	

[a] KS: [*Kaneko and Shearer*, 2014], Ma: [*Madariaga*, 1976], SH: [*Sato and Hirasawa*, 1973] and B: [*Brune*, 1970]. The models labeled with stars are from the current study (their fonts are bold), and k^P and k^S are the parameters derived for those models.

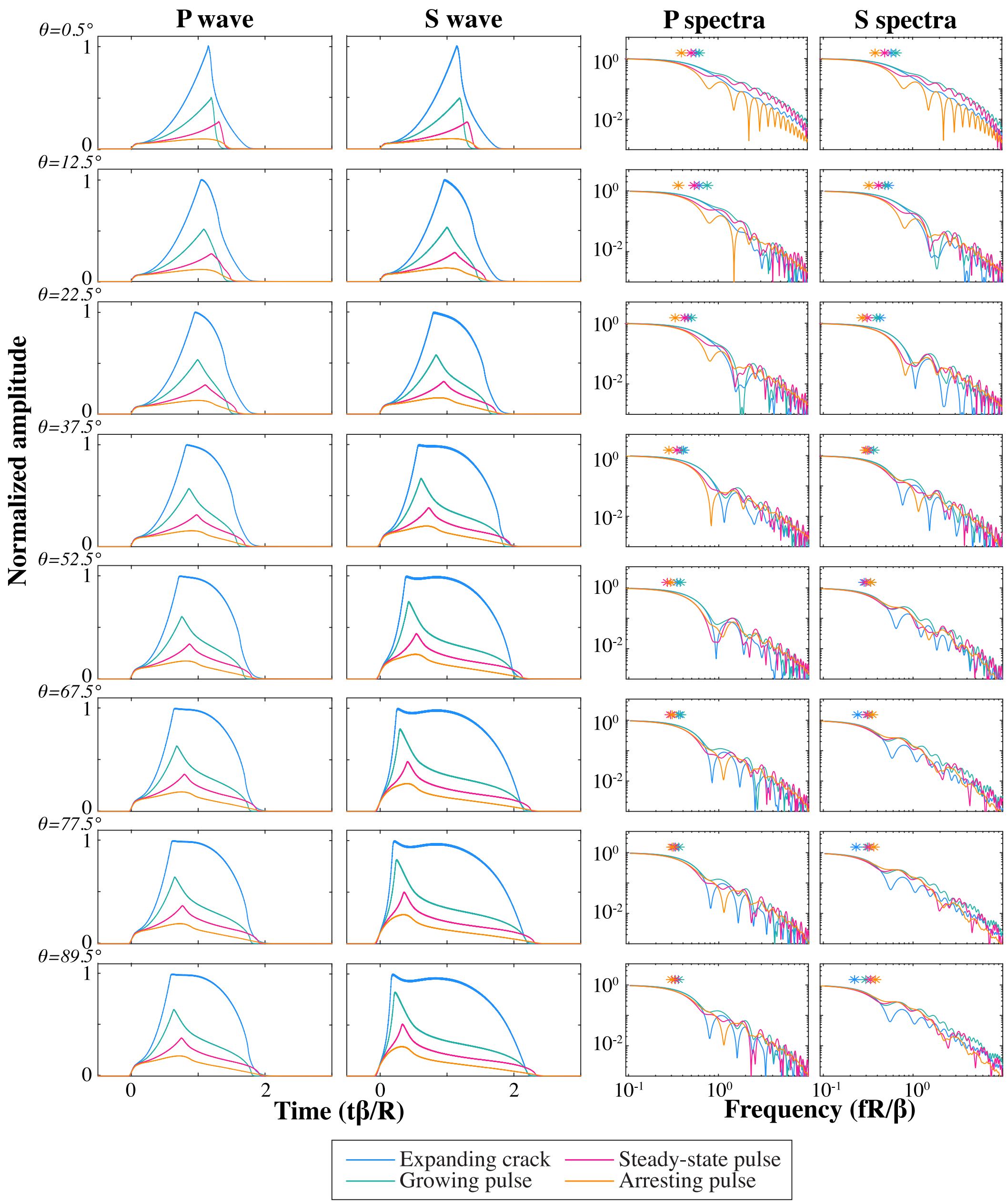

358 **Figure 8.** The radiated P and S displacement and spectra at 8 take-off angles from 4 dynamic rupture
359 models (denoted by 4 colors). Best fit corner frequency f_c of each spectrum is indicated by a star.

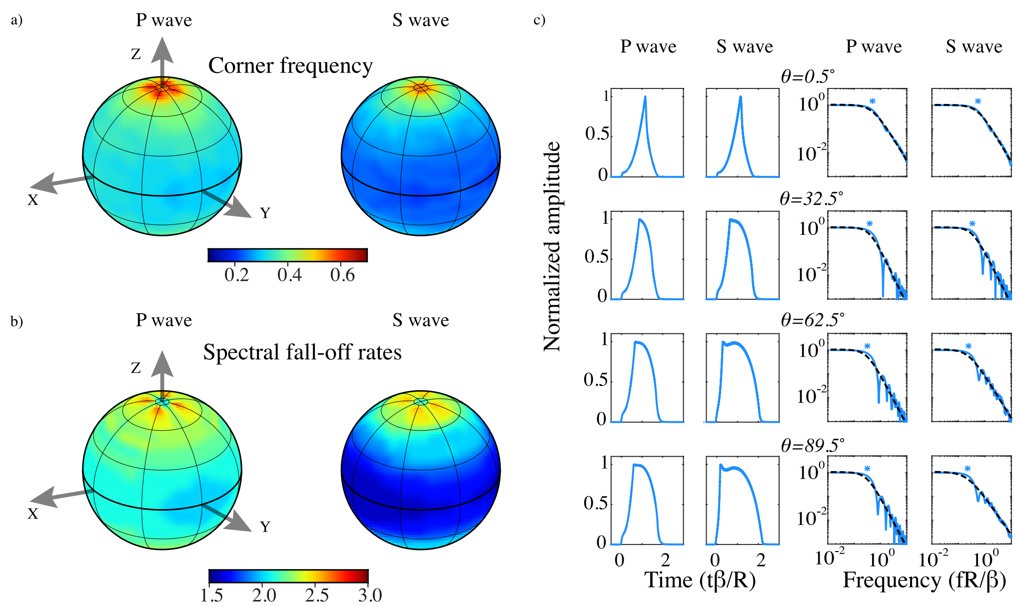

Figure 9. Far-field displacements, spectra, normalized corner frequencies ($f_c R/\beta$) and fall-off rates for expanding crack model. (a) Distributions of P and S spectral corner frequencies ($f_c R/\beta$) over the focal sphere. X and Y axes are identical with those in Figures 4-7. (b) Distributions of P and S spectral fall-off rate over the focal sphere. (c) 4 sampled displacements and spectra of P and S waves. Black dashed lines are best fit Brune model and star symbol denotes best fit corner frequency.

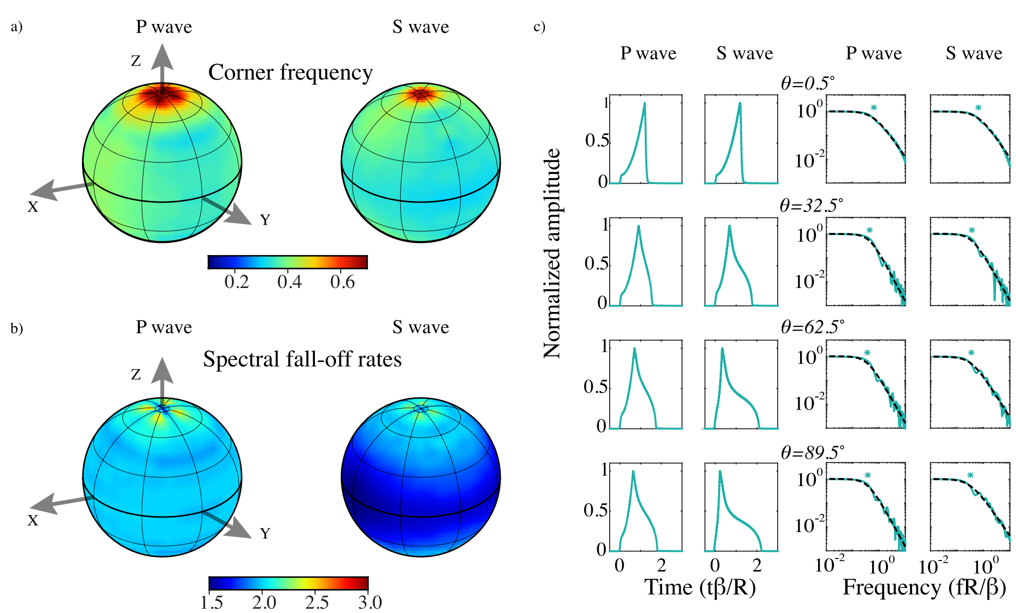

Figure 10. Far-field displacements, spectra, normalized corner frequencies and fall-off rates for growing pulse model. (a) Distributions of P and S spectral corner frequencies over the focal sphere. (b) Distributions of P and S spectral fall-off rate over the focal sphere. (c) 4 sampled displacements and spectra of P and S waves. Black dashed lines are best fit Brune model and star symbol denotes best fit corner frequency.

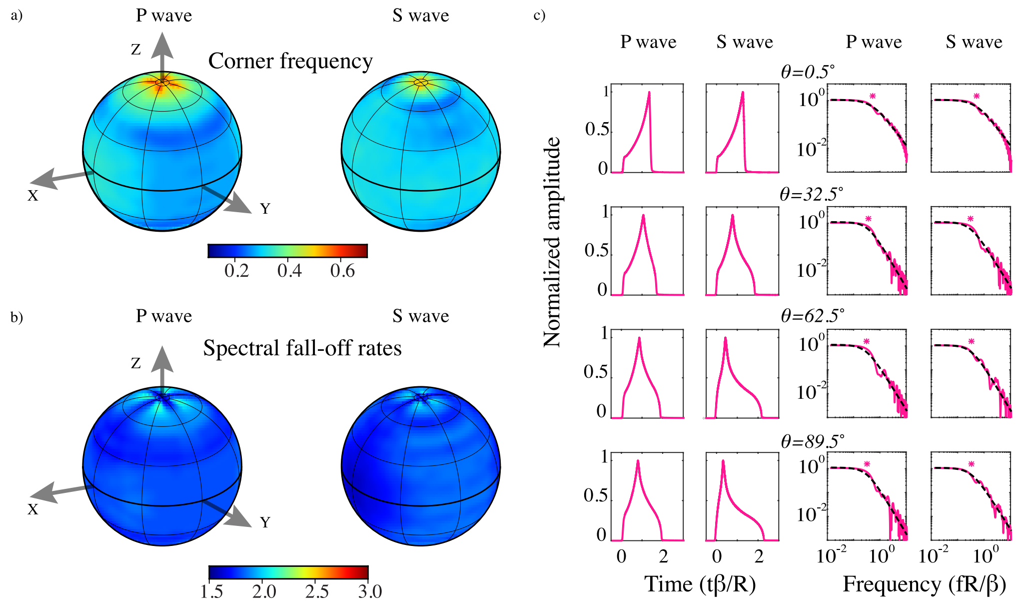

475 **Figure 11.** Far-field displacements, spectra, normalized corner frequencies and fall-off rates for steady-state
476 pulse model. (a) Distributions of P and S spectral corner frequencies over the focal sphere. (b) Distributions
477 of P and S spectral fall-off rate over the focal sphere. (c) 4 sampled displacements and spectra of P and S
478 waves. Black dashed lines are best fit Brune model and star symbol denotes best fit corner frequency.

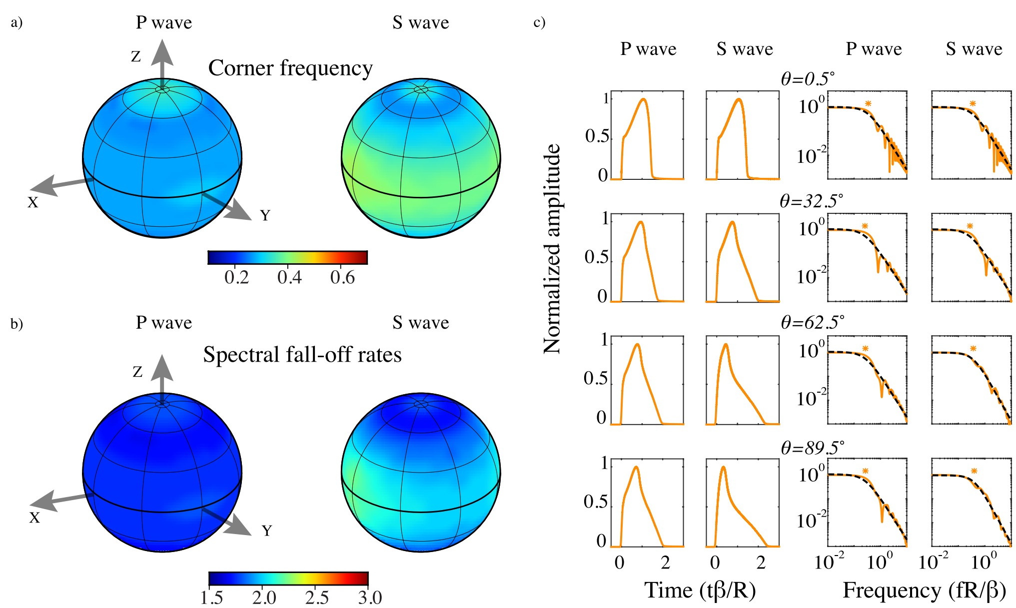

501 **Figure 12.** Far-field displacements, spectra, normalized corner frequencies and fall-off rates for arresting
502 pulse model. (a) Distributions of P and S spectral corner frequencies over the focal sphere. (b) Distributions
503 of P and S spectral fall-off rate over the focal sphere. (c) 4 sampled displacements and spectra of P and S
504 waves. Black dashed lines are best fit Brune model and star symbol denotes best fit corner frequency.

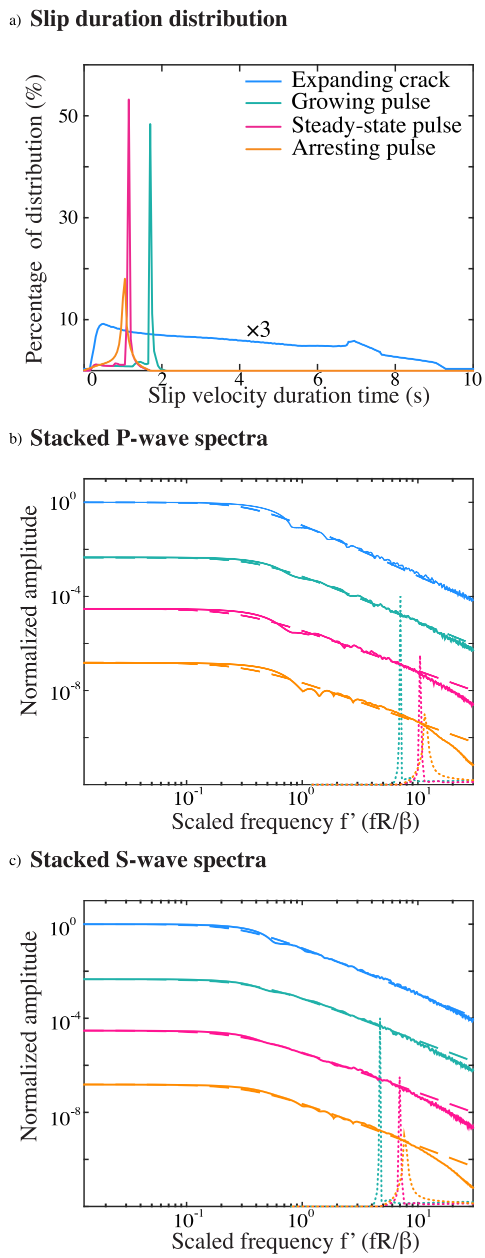

Figure 13. Slip rate duration distribution and stacked spectra of P and S waves for each model. (a) The distributions of slip rate durations for each model (we scale the curve of expanding crack with a factor of 3 to highlight the linearly decreasing distribution of slip duration). (b) Stacked P wave spectra (solid lines) and best fitted Brune model (dashed lines). Dotted curves are frequency distribution of K/T, with K scaled such that K/T is a rough indicator of the second corner frequency. (c) Stacked S wave spectra and best fit Brune model.

Double corner frequency spectra are common in both theoretical and empirical seismic studies. Kinematically, the lower and higher corner frequencies typically correspond to rupture duration (controlled by fault dimension) and slip rise time (duration of the slip-velocity pulse), respectively [e.g. *Ben-Menahem*, 1962; *Haskell*, 1964]. Physically, the explanation of the secondary corner in our pulse-like models is similar in spirit to the partial stress-drop model suggested by *Brune* [1970]. In Brune's partial-stress-drop model (in contrast to the conventional Brune model), slip is hypothesized to be arrested early, such that static stress drop is less than dynamic stress drop, which is what occurs in our pulse-like spontaneous rupture models (and similar behavior is implicit in some barrier and asperity models [e.g. *Boatwright* , 1984; *Uchide and Imanishi*, 2016]). The development of slip pulses was previously related to the occurrence of a secondary spectral corner in the numerical modeling of *Shaw* [2003]. Numerous observational studies have proposed double corner frequency spectral models [e.g. *Atkinson and Silva*, 1997], and the issue deserves renewed attention in light of observational results such as those of *Denolle and Shearer* [2016] documenting a systematic emergence of a secondary spectral corner for the largest events in the global dataset and *Archuleta and Ji* [2016] documenting a break in scaling of LogPGA and LogPGV versus moment magnitude **M** around **M** ∼ 5.3.

Anticipating that the second corner frequency can be related to slip rise time (by analogy with the Haskell fault model), we investigate the distributions (histograms) of slip duration for each model (Figure 13a). In Figure 13a, the ordinate gives the percentage of the total rupture area having slip-rate duration within the 0.5 second wide bin centered at the abscissa value. The expanding crack model has a very broad distribution of slip duration over the interval from 0.5s to 10s (the curve of the expanding crack is scaled by a factor of 3 to highlight this feature in Figure 13a), but all of the pulse-like ruptures have relatively narrow distributions of slip duration. This can be partially understood as a result of a diminished influence of the overall rupture geometry for pulse-like ruptures compared with crack-like modes; both total slip and slip velocity of these pulse-like ruptures are controlled principally by local shear stress and frictional properties rather than by global rupture features such as rupture edge diffractions. We assume that the second corner frequency scales inversely with the mean slip duration time:

$$f_c^{2nd} = \frac{K}{\overline{T}}, \tag{19}$$

where $\overline{T}$ is mean slip velocity duration and K is a constant to be determined. In Figure 13b and 13c, solid and dashed lines are spectral stacks computed from the simulations and Brune's model spectra, respectively. The presence of a second corner frequency shows up as a clear departure from the constant spectral slope of the Brune model. The dotted lines in Figures 13b and 13c are curves of K/T distribution derived from Figure 13a, for a fixed value of K for each wave type (around 1.8 and 1.5 for P and S wave respectively) that was determined, by trial and error adjustment, such that the distribution peak (from the dashed curves) coincides with the lowest frequency where the spectral stack departs visibly from the best fit Brune model. The proportionality between this frequency and $\overline{T}$ confirms, unsurprisingly, that, if a secondary corner frequency is interpreted in terms of pulse-like rupture, its value provides an estimate of mean slip duration. The upper spectral asymptote is not well determined in the simulations, however, so this estimate of K provides only a lower bound on the value of the second corner frequency (where the latter is defined as the frequency of intersection of the intermediate and upper spectral asymptotes), and thus may not be directly comparable with other K estimates (for example, a similar parameter in *Savage* [1972] equals 1 and in *Denolle and Shearer* [2016] equals $1/\pi$).

As the rupture model evolves from a growing- to an arresting-pulse mode, the spectral decay above the second corner becomes steeper, as seen in Figures 13b and 13c. This transition reflects the relative suppression of stopping phases, especially in the decaying pulse model, consistent with the expected dominance of stopping phases in the high-frequency limit [*Madariaga*, 1976, 1977b]. In the presence of the second corner and increased rate of high-frequency decay, fitting over a broad frequency band to the conventional, single corner frequency Brune spectral function can bias the estimate of the first corner frequency, leading to uncertainties and bias in the stress drop estimate. For example, for shallow thrust earthquakes, *Denolle and Shearer* [2016] find that the conventional Brune model with a single-corner frequency is unable to fit spectra for high-magnitude events, and a double-corner frequency model improves the fitting and gives more consistent estimates of the first corner frequency in the sense that the subsequent stress drop estimates are roughly invariant with seismic moment (given additional scaling assumptions, i.e., the length to width scaling of *Leonard* [2010]).

7 Energy Partitioning and Stress Drop

The partitioning of radiated energy between P and S waves is rupture-model dependent, and we use our four source models to show the effect of rupture mode on the P/S energy ratio. Radiated energy can be calculated from each simulation using fault-plane stresses and velocities via [*Rudnicki and Freund*, 1981]

$$E_r = \iint \frac{\tau_0 + \tau_f}{2} \Delta u dS - \int_0^\infty \iint \tau(t) \Delta \dot{u}(t) dS dt, \tag{20}$$

where $\Delta \dot{u}$ is the slip velocity, τ_0 and τ_f are initial and final shear stress and $\tau(t)$ is the shear stress as a function of time. The corresponding estimate of radiated energy from far-field body-wave displacements is

$$E_r' = \rho \int_0^\infty \oiint [\alpha (V^P)^2 + \beta (V^S)^2] d\Sigma dt, \tag{21}$$

where V^P and V^S are far-field velocities of P and S waves, the integration is over a sphere surrounding the fault and the prime symbol here denotes the parameter derived from far-field observations instead of from the fault surface. Before considering the P and S contributions separately, we first verify the internal consistency of our calculations by comparing estimates (20) and (21) for the total energy. These two energy estimates, for each source model, are listed in Table 4, and show differences of the order of 1 or 2% (which we attribute to errors from focal-sphere sampling, together with effects of the small artificial viscosity used in the simulations and neglected in the energy balance calculations) verifying the self-consistency of the far-field and on-fault estimates.

The computed P and S radiated energies for the crack-like and pulse-like rupture models are shown in Table 4. The P/S ratio for the crack-like rupture mode, 20, is similar to values of 24.4 for the analytical model of *Sato and Hirasawa* [1973] and 21.8 for the numerical model of *Kaneko and Shearer* [2014]. The S/P energy ratio is larger for pulse-like ruptures than for the crack-like case, and larger for growing and steady-state pulses than for the arresting pulse rupture mode. This pattern mirrors the behavior of the radiation ratio η_R [*Noda et al.*, 2013], also shown in Table 4, and examined further in the Discussion section. We also note that our radiated energy ratios differ markedly from what would be predicted if the rms P- and S-wave spectral shapes were scaled (both amplitude and frequency axes) versions of each other (something also noted by *Kaneko and Shearer* [2014]). As shown by *Boatwright and Fletcher* [1984], the latter estimate is

$$\frac{E_r^S}{E_r^P} = 1.5 (\frac{\alpha}{\beta})^5 (\frac{f_c^S}{f_c^P})^3. \tag{22}$$

As Table 4 shows, this estimate under-predicts the energy ratio of the crack-like model by about a factor of two and over-predicts that of the arresting pulse model by a similar factor.

Fault slip and stresses from the simulations provide two complementary measures of average stress drop, denoted $\Delta\sigma_E$ and $\Delta\sigma_M$ by *Noda et al.* [2013]. The former is the

Table 4. Comparison energy partitioning and static stress drop among 4 models.

	Expanding crack	Growing pulse	Steady-state pulse	Arresting pulse
Radiated Energy				
$\underline{\mathbf{E_r}}(10^{15}\mathrm{J})$	21.01	9.29	2.92	1.14
$E_r'(10^{15}\mathrm{J})$	20.89	9.17	2.88	1.12
Ratio between E_r^S and E_r^P				
$\underline{\mathbf{E_r^S/E_r^P}}$	20	29	27	24
E_r^S/E_r^P*	11	18	23	46
Static stress drop				
$\underline{\mathbf{\Delta\sigma_E}}(\mathrm{MPa})$	15.69	9.37	6.41	5.53
$\underline{\mathbf{\Delta\sigma_M}}(\mathrm{MPa})$	15.66	7.13	4.61	3.36
Radiation ratio				
$\underline{\eta_{\mathbf{R}}}$	0.40	0.65	0.46	0.41

All parameters underlined are computed directly from fault-plane stresses and slip from the numerical simulations. Parameters labeled with $'$ are derived from far-field displacements or spectra calculated from the simulations. The energy ratio labeled with * represents results from Eq-22 [*Boatwright and Fletcher*, 1984].

average static stress drop weighted by the final slip,

$$\Delta\sigma_E = \frac{\iint \Delta\sigma\Delta u dS}{\iint \Delta u dS}, \tag{23}$$

where $\Delta\sigma$ is the static stress drop as a function of position on the fault surface. As *Shao et al.* [2012] point out, $\Delta\sigma_E$ is just twice the ratio of so-called "available elastic energy" [*Kanamori and Rivera*, 2006] to the seismic potency. Values obtained directly from Eq-23 are listed in Table-4. An alternative measure, called moment-based stress drop [*Noda et al.*, 2013] is stress drop weighted by the slip distribution E due to a (hypothetical) uniform stress drop on the same fault surface,

$$\Delta\sigma_M = \frac{\iint \Delta\sigma E dS}{\iint E dS}. \tag{24}$$

For the circular rupture, Eq-24 gives the standard formula Eq-3, with the left-hand side interpreted now as $\Delta\sigma_M$ (and a similar expression can be derived for an elliptical rupture). The corresponding values of $\Delta\sigma_M$ for the simulations are listed in Table-4 for comparison with $\Delta\sigma_E$ values. If Eq-3 is applied, with rupture radius R estimated from corner frequency (Eq-4) using a crack-like model for k, those radius estimates will be biased for the pulse-like models by the ratio of the crack- to pulse-like k values in Table 3 (i.e., factors of 0.87, 1.13, and 1.25 for P waves, and 0.75, 0.87, and 0.8 for S waves, for growing, steady-state, and arresting pulse, respectively). Subsequently using Eq-3 to estimate stress drop from radius would lead to stress drop biased by the cube of those factors (Eq-5), if the relationship between mean slip (or moment) and stress drop followed the crack-like model like Eq-1 or 3. However, actual biases in the stress drop estimates are generally more complex than that, because the relationship between mean slip and stress drop also becomes modified for pulse-like ruptures.

We can examine the variability in spectral estimates of stress drop resulting from presumably unknown variations in rupture mode. Using values of k^P and k^S from each of four crack-like models (1. *Madariaga* [1976], 2. *Kaneko and Shearer* [2014], 3. *Brune* [1970], and the expanding crack model of the current study), we make "blind" stress drop ($\Delta\sigma_M$) estimates from spectral parameters M_0 and f_c obtained from the growing, steady-state, and arresting pulse models, respectively. These estimates are denoted $\Delta\sigma_{Ma}$, $\Delta\sigma_{KS}$, $\Delta\sigma_B$, and $\Delta\sigma_{crack}$, respectively. Results for the four stress drop estimates, normalized by each of the actual stress drops $\Delta\sigma_M$ of the pulse-like ruptures (from Table 4) are shown in Figure 14. For P-wave estimates, the rupture mode introduces over- and under-estimates ranging over roughly a factor of two either way. The S-wave estimates have a somewhat larger range, due to a substantial overestimate of $\Delta\sigma_M$ by the *Madariaga* [1976] model.

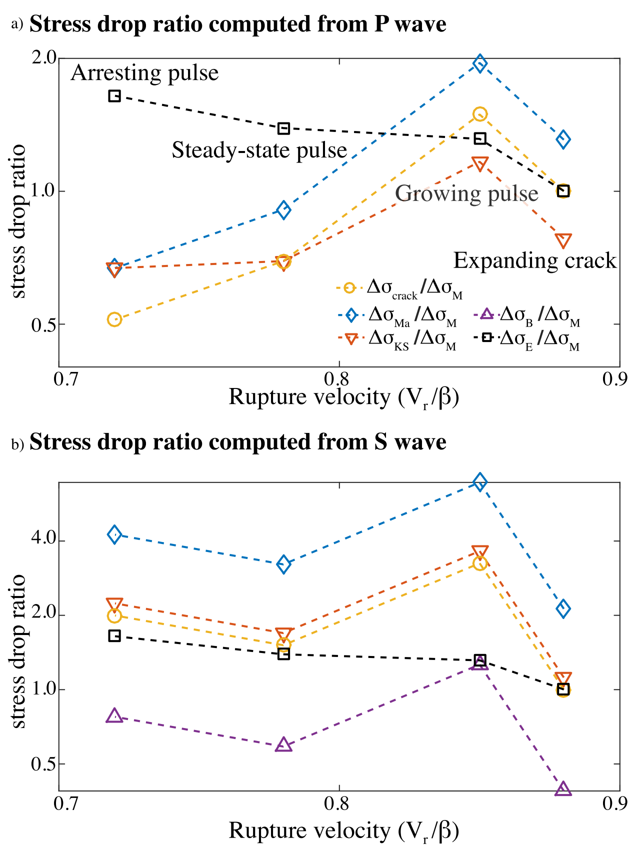

Figure 14. The ratio between spectrally estimated stress drop and actual moment-based stress drop for the 4 simulated rupture models. Four sets of parameters, k^P and k^S are used to investigate how large the variabilities of estimations can be. The vertical axis is logarithmic. Also shown is the ratio between $\Delta\sigma_E$ and $\Delta\sigma_M$ for each simulation, denoted by black squares, demonstrating the divergence of these two averages as rupture mode changes from crack-like to pulse-like.

The S wave estimates based on *Kaneko and Shearer* [2014] and the crack-like model of the current study are very similar, each biased high by about a factor of two for the pulse-like ruptures, and each showing about a factor of two variability about that factor. The upward bias is what would be expected as a consequence of the S-wave rupture radius underestimates noted above. That upward bias is sharply reduced, however, when we compare with $\Delta\sigma_E$ (open squares in Figure 14) instead of $\Delta\sigma_M$, since both spectral estimates $\Delta\sigma_{KS}$ ([*Kaneko and Shearer*, 2014]) and $\Delta\sigma_{crack}$ (current study) represent quite accurate $\Delta\sigma_E$ values for the steady-state and arresting pulse ruptures. The Brune estimate is low for the crack-like rupture model, but within plus/minus 40% for the pulse-like ruptures.

This reduction of bias when bias is taken relative to $\Delta\sigma_E$ is a result of the differences in spatial distribution of slip of the pulse- versus crack-like models. For the pulse-like models, $\Delta\sigma_E$ exceeds $\Delta\sigma_M$, with the excess being related to the level of heterogeneity of stress drop [*Noda et al.*, 2013]. As indicated in Table 4 and Figure 14, $\Delta\sigma_E$ and $\Delta\sigma_M$ for the expanding crack are nearly identical as expected. However, in pulse-like ruptures, $\Delta\sigma_M$ is 24%, 28% and 40% smaller than $\Delta\sigma_E$ in growing, steady-state and arresting pulse, respectively. Such a phenomenon is similarly observed in [*Noda et al.*, 2013]. The reason is that the healing of the pulse-like rupture freezes in the static slip before it reaches the elliptic shape of the circular static crack, which has the form [*Eshelby*, 1957]:

$$\Delta u(l) = I\sqrt{R^2 - l^2}[1 - H(l - R)], \tag{25}$$

where I is a constant proportional to the stress drop, R is the rupture radius, l is the distance to hypocenter and H is a Heaviside function. In Figure 15, the dashed and solid lines denote the best fit solutions of the form of Eq-25 and the simulated models (shown along the inplane direction), respectively. As expected, the crack-like rupture model closely follows the Eshelby solution, consistent with the close agreement we found between $\Delta\sigma_M$ and $\Delta\sigma_E$. The pulse-like model deviates much more from the Elshelby solution, with the main difference being weaker dependency of slip on hypocentral distance (apart from the region right around the nucleation patch). The resulting contrast in spatial patterns of slip between crack- and pulse-like rupture elevates $\Delta\sigma_E$ relative to $\Delta\sigma_M$ in the pulse-like case.

8 Discussion

The slip-pulse durations in our models are mostly in the range of 1-2 seconds (Figure 13a). This range is also representative of slip-pulse durations inferred in observational studies, at least for shallow crustal earthquakes [e.g. *Heaton*, 1990; *Somerville et al.*, 1999]. The source dimension of our simulations is such that the secondary corner introduced by the occurrence of these pulse-like ruptures only affects the spectral shape at frequencies exceeding the lower corner frequency by at least a factor of 20. The spectral fitting procedure used here (motivated by standard observational practice) appears to provide reliable estimates of the lower corner frequency and the intermediate spectral slope in this case, since the frequency band used in fitting, $0.05f_c < f < 20f_c$, is entirely below the higher corner frequency. As indicated in Figure 16, further narrowing the frequency band to $0.05f_c < f < 10f_c$, as in *Kaneko and Shearer* [2014, 2015] only slightly alters the spectral fit, (and only at low take-off angles). The use of the narrower band suppresses some of the azimuthal variation in the corner-frequency distribution (e.g., near the z axis in Figure 11a), but has little effect on the averaged values, which are summarized in Table 5. Compared with the results from the narrower band, k and n estimates from the broader band differ by a maximum of around 10% and 12% respectively (comparing Tables 2 and 5). When we increase the upper frequency limit to $30f_c$ (very near to the second corner frequency), there is no significant change in the estimates of k and n. In summary, the results are fairly insensitive to our choice the spectral range, although this conclusion depends upon the fact that the rupture dimension in the models was large enough to provide good separation between the corner frequencies.

In observational studies, there exists great variability in estimates of earthquake parameters derived from seismic spectra, such as stress drop and radiated energy. Simulations, for which the earthquake parameters are precisely known (from near-field calculations) are a valuable aid in the interpretation of spectra in terms of earthquake parame-

Table 5. Spectral parameters of P and S waves for the 4 models obtained, using modified frequency band $0.05f_c < f < 10f_c$

	Expanding crack	Growing pulse	Steady-state pulse	Arresting pulse
V_r^2	0.88β	0.85β	0.78β	0.72β
V_r^3	0.84β	0.81β	0.74β	0.66β
k^P	0.38	0.40	0.32	0.30
k^S	0.29	0.35	0.32	0.34
$\frac{k^P}{k^S}$	1.3	1.1	1.0	0.9
n^P	2.3	2.0	1.9	1.9
n^S	2.0	1.7	1.8	1.9
k^P_{stack}	0.40	0.43	0.34	0.30
k^S_{stack}	0.31	0.38	0.32	0.32
$\frac{k^P_{stack}}{k^S_{stack}}$	1.3	1.1	1.1	1.0
n^P_{stack}	2.3	2.0	1.9	1.9
n^S_{stack}	2.0	1.8	1.8	1.9

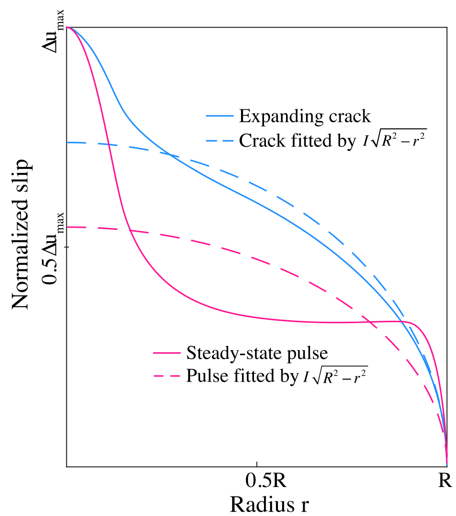

Figure 15. Slip distribution, comparing crack-like and pulse-like models. The blue solid and dashed lines are the final slip distribution from expanding crack model and best fitted Eshelby's solution. The pink solid and dashed lines are the final slip distribution from expanding crack model and best fit Eshelby solution. In both sets of lines, the degree of discrepancy between obtained models and the theoretical static solution determines the appropriateness of conventional Eq-1 or Eq-3 for computing static stress drop. The misfit at small radius is due to the nucleation effect (different stress drop in the nucleation zone).

ters and can provide useful insight into the origin of the variability of spectrally-derived estimates. Our analysis of the spectral consequences of the rupture type transition from classic crack-like to pulse-like mode may have application in the estimation of earthquake parameters for particular earthquakes. For example, we may be able to sharpen some parameter estimates in cases where we have independent evidence of rupture mode, e.g., from finite-fault inversion. In such cases, our results for empirical parameters k^P and k^S (section 5) and for the effect of pulse-like rupture on stress drop estimation (Section 7) may be used to refine spectral estimates of source parameters. Likewise, the spectral fall-off rates (n^P and n^S) could help refine frequency-domain radiated energy estimates (obtained by the application of Parseval's theorem to Eq-21), which are highly dependent on presumed spectral shapes (e.g., [*Hirano and Yagi*, 2017]). In other cases, absent detailed kinematic inversion results (especially for small to intermediate earthquakes), rupture types are usually unknown to us. In those cases, the results (Section 6) showing double corner frequency spectral shapes of pulse-like models may provide interpretive guidance. For example, *Denolle and Shearer* [2016] find a double corner frequency model fits their analysis of large, shallow thrust earthquakes, and since the upper corner appears to be too high in frequency to be related to a fault dimension, a possible interpretation would relate the upper corner to slip pulse duration (and *Denolle and Shearer* [2016] discuss other interpretations). Future work resolving higher frequency spectral properties, may provide more quantitative constraints on the association of pulse width with the second corner frequency, the extent to which pulse width may scale with other parameters (e.g., moment), and the asymptotic decay slope for pulse-like ruptures.

As noted earlier, the simulations provide precise values of radiated energy, seismic moment and static stress drop for all the rupture models, and this enables us to consider

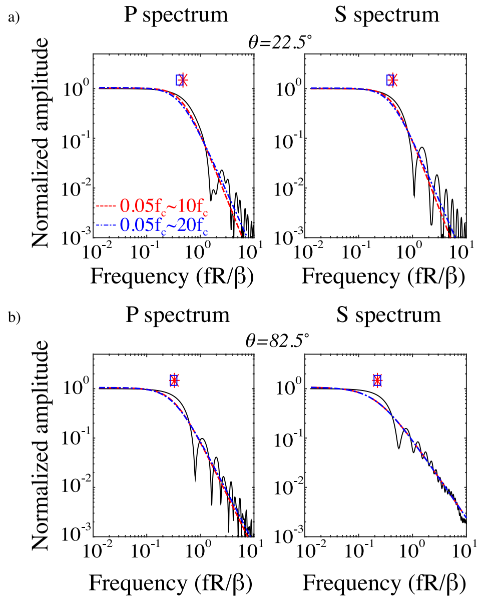

Figure 16. Effect of frequency band on spectral fitting. (a) Black solid lines are P and S spectrum at 22.5° take-off angle. The red and blue dashed lines are best fit Brune model using $0.05 f_c \sim 10 f_c$ and $0.05 f_c \sim 20 f_c$, respectively. At low take-off angle, slight difference of fitting occurs at high frequency. (b) Black solid lines are P and S spectrum at 82.5°. The red and blue dashed lines are best fit Brune model using $0.05 f_c \sim 10 f_c$ and $0.05 f_c \sim 20 f_c$, respectively. At high take-off angle, both bands result in identical fitting.

the implications of rupture mode for other quantities derived from these source parameters. The radiation ratio (we follow the terminology of *Noda et al.* [2013] for what is sometimes called the radiation efficiency, though its value can exceed 1), defined as

$$\eta_R = \frac{2\mu E_R}{M_0 \Delta\sigma_E}, \tag{26}$$

is an interesting example, and values are compiled in Table 4 and shown in Figure 17a (red triangles). It is required to clarify that the static stress drop here denotes $\Delta\sigma_E$ because in considering energy partitioning, we need energy-based stress drop estimates instead of moment-based estimates ($\Delta\sigma_M$) although they are not easy to seismologically distinguish them. The blue star symbol denotes the average amplitude of the final slip spatial gradient, which can serve as a good indicator of rupture type (the small value of slip gradient implies flat slip distribution, as in the more pulse-like ruptures, and the large value denotes crack-like mode. Its mathematical expression is $\int_L |\frac{d\Delta u(x)}{dx}| dl/L$ in which L is rupture length along the inplane direction (X), l is the distance variable and Δu is the slip function). When the rupture type transits from pulse-like to crack-like (from left to right in Fig 17a), the radiation ratio initially increases, has a maximum for the growing pulse case, and then falls for the crack-like case. This behavior is probably a consequence of the undershoot of the static stress drop, relative to the maximum dynamic stress drop, in pulse-like models, as seen in Figure 3b. To verify that this dependence of radiation ratio on rupture mode is not specific to our method of inducing the rupture mode transition (via scaling of V_w), we do a similar set of simulations, but inducing the transition from pulse-like to crack-like modes by raising initial shear stress (with V_w fixed). We also add more simulations (a total of 22) to refine the resolution of the rupture-mode transition. The results, shown in Figure 17b, confirm that the transition of rupture from decaying to growing pulse-like behavior is associated with a large (up to factor of 1.6), systematic increase in radiation ratio, and that the transition to crack-like rupture corresponds to an equally large drop in radiation ratio (the small increases in efficiency for the highest initial-stress case is associated with a supershear rupture transition).

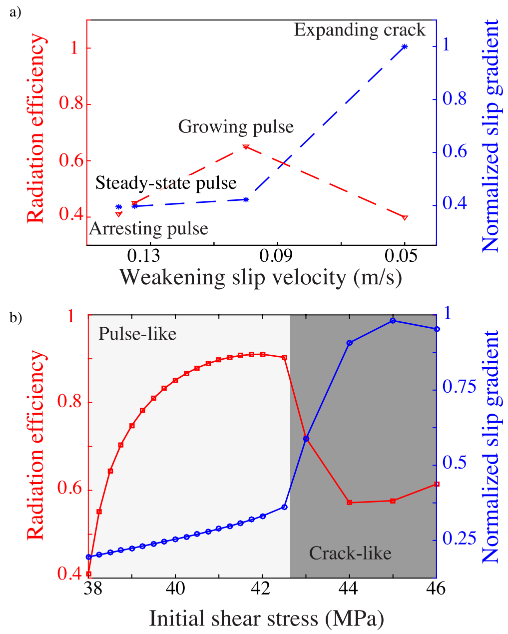

Figure 17. Radiation ratio variation with rupture mode transition. (a) radiation ratio (red dashed line) and slip gradient (rupture type indicator, blue dashed line) of 4 models show with rupture mode is changed to crack-like, radiation ratio has an apparent reduction. (b) Similar pattern can be observed when we switch to adjust initial shear stress to regenerate a rupture mode transition.

9 Conclusions

Spontaneous rupture simulations with rate and state friction and dynamic weakening show a rupture mode transition from crack- to pulse-like under adjustment of the critical weakening velocity V_w. Four representative models provide a basis for examining the effect of rupture mode on source parameter estimates: an expanding crack, a growing pulse (increasing peak slip velocity with rupture radius), a steady-state pulse (nearly constant peak slip velocity), and an arresting pulse (with spontaneous rupture termination). Relative to a crack-like rupture with similar geometry, a pulse-like rupture leads to additional complexity in the far-field displacement spectra, including a double corner-frequency structure, with the higher corner frequency inversely proportional to pulse duration. The focal-sphere-averaged lower P and S wave corner frequencies (normalized to source dimension) are systematically higher for pulse-like models than for crack models of comparable rupture velocity (Table 3), while the lower P-wave corner is less sensitive to rupture mode. The P/S corner frequency ratio also varies systematically with rupture mode, from ~1.3 for the crack model to ~0.9 for the arresting pulse (Table 2). The spectral slope (above the lower corner) in most cases is only slightly affected by rupture mode; in nearly all cases, this slope is in the range -2 ± 0.2, with the P spectral slope more sensitive to rupture mode than the S slope (Table 2).

The slip-weighted stress drop $\Delta\sigma_E$ exceeds the moment-based stress drop $\Delta\sigma_M$ for pulse-like ruptures, with the ratio ranging from about 1.3 to 1.65, while they are equal for the crack-like case. The variations in rupture mode modeled in this study introduce variability of the order of a factor of two in standard (i.e., crack-model based) spectral estimates of stress drop, accompanied by some systematic bias. The S-wave spectral estimates for the pulse-like ruptures are biased high by about a factor of two when stress drop is interpreted as $\Delta\sigma_M$, but show little bias when stress drop is interpreted as $\Delta\sigma_E$ (and P-wave estimates show less systematic bias). The transition from arresting- to growing-pulse rupture is accompanied by a large (factor of ~1.6) increase in the radiation ratio ("radiation efficiency"), with a comparable drop in that ratio at the transition from growing-pulse to crack-like rupture. Thus, variations in rupture mode may account for portion of the scatter in observational spectral estimates of source parameters, and, in instances in which independent constraints on rupture mode are available, the results derived here (in particular, values for rupture style-dependent normalized corner frequencies k^P and k^S and spectral slopes n^P and n^S) may help sharpen those estimates.

Acknowledgments

The authors thank Peter Shearer, Marine Denolle and Yoshihiro Kaneko for the helpful discussions and suggestions. We also thank Editor Yehuda Ben-Zion, Associate Editor, Ralph Archuleta and an anonymous reviewer for their constructive comments that improved this manuscript. The simulations were performed on Blue Waters at the National Center for Supercomputing Applications (NCSA). This work was supported by NSF award EAR-1135455.

References

Abercrombie, R. E. (1995), Earthquake source scaling relationships from -1 to 5 ML using seismograms recorded at 2.5-km depth, *J. Geophys. Res.*, *100*(B12), 24,015–24,036, doi:10.1029/95JB02397.

Aki, K., and P. G. Richards (2002), *Quantitative Seismology*, University Science Books, Sausalito, Calif.

Allmann, B. P., and P. M. Shearer (2007), Spatial and temporal stress drop variations in small earthquakes near Parkfield, California, *J. Geophys. Res.*, *112*, doi: 10.1029/2006jb004395.

Allmann, B. P., and P. M. Shearer (2009), Global variations of stress drop for moderate to large earthquakes, *J. Geophys. Res.*, *114*, doi:10.1029/2008jb005821.

Ampuero, J. P., and Y. Ben-Zion (2008), Cracks, pulses and macroscopic asymmetry of dynamic rupture on a bimaterial interface with velocity-weakening friction, *Geophys. J. Int.*, *173*(2), 674–692, doi:10.1111/j.1365-246X.2008.03736.x.

Andrews, D. J., and Y. Ben-Zion (1997), Wrinkle-like slip pulse on a fault between different materials, *J. Geophys. Res.*, *102*(B1), 553–571, doi:10.1029/96JB02856.

Archuleta, R. J., and C. Ji (2016), Moment rate scaling for earthquakes 3.3≤M≤5.3 with implications for stress drop, *Geophys. Res. Lett*, *43*, 12,004–12,011, doi: 10.1002/2016GL071433.

Archuleta, R. J., E. Cranswick, C. Mueller, and P. Spudich (1982), Source parameters of the 1980 Mammoth Lakes, California, earthquake sequence, *J. Geophys. Res.*, *87*(B6), 4595–4607, doi:10.1029/JB087iB06p04595.

Atkinson, G. M., and W. Silva (1997), An empirical study of earthquake source spectra for California earthquakes, *Bull. Seismol. Soc. Am.*, *87*(1), 97–113.

Baltay, A., S. Ide, G. Prieto, and G. Beroza (2011), Variability in earthquake stress drop and apparent stress, *Geophys. Res. Lett*, *38*, doi:10.1029/2011GL046698.

Baltay, A. S., and T. C. Hanks (2014), Understanding the magnitude dependence of PGA and PGV in NGA-West 2 data, *Bull. Seismol. Soc. Am.*, *104*(6), 2851–2865.

Baumann, C., and L. A. Dalguer (2014), Evaluating the compatibility of dynamic rupture-based synthetic ground motion with empirical ground-motion prediction equation, *Bull. Seismol. Soc. Am.*, *104*(2), 634–652.

Beeler, N. M., and T. E. Tullis (1996), Self-healing slip pulses in dynamic rupture models due to velocity-dependent strength, *Bull. Seismol. Soc. Am.*, *86*(4), 1130–1148.

Ben-Menahem, A. (1962), Radiation of seismic body waves from a finite moving source in the earth, *J. Geophys. Res.*, *67*(1), 345–350, doi:10.1029/JZ067i001p00345.

Ben-Zion, Y., T. K. Rockwell, Z. Q. Shi, and S. Q. Xu (2012), Reversed-polarity secondary deformation structures near fault stepovers, *J. Appl. Mech.*, *79*(3), 031025, doi:10.1115/1.4006154.

Beroza, G. C., and T. Mikumo (1996), Short slip duration in dynamic rupture in the presence of heterogeneous fault properties, *J. Geophys. Res.*, *101*(B10), 22,449–22,460, doi:10.1029/96JB02291.

Boatwright, J., and J. B. Fletcher (1984), The partition of radiated energy between P-wave and S-wave, *Bull. Seismol. Soc. Am.*, *74*(2), 361–376.

Boatwright, J. (1988), The seismic radiation from composite models of faulting, *Bull. Seismol. Soc. Am.*, *78*(2), 489–508.

Boore, D. M. (1983), Stochastic simulation of high-frequency ground motions based on seismological models of the radiated spectra, *Bull. Seismol. Soc. Am.*, *73*(6), 1865–1894.

Brune, J. N. (1970), Tectonic stress and spectra of seismic shear waves from earthquakes, *J. Geophys. Res.*, *75*(26), 4997–5009, doi:10.1029/JB075i026p04997.

Brune, J. N., R. J. Archuleta, and S. Hartzell (1979), Far-field S-wave spectra, corner frequencies, and pulse shapes, *J. Geophys. Res.*, *84*(B5), 2262–2272, doi:10.1029/JB084iB05p02262.

Cochard, A., and R. Madariaga (1996), Complexity of seismicity due to highly rate-dependent friction, *J. Geophys. Res.*, *101*(B11), 25,321–25,336, doi:10.1029/96JB02095.

Dahlen, F. A. (1974), On the ratio of P-wave to S-wave corner frequencies for shallow earthquake sources, *Bull. Seismol. Soc. Am.*, *64*(4), 1159–1180.

Dalguer, L. A., and S. M. Day (2009), Asymmetric rupture of large aspect-ratio faults at bimaterial interface in 3D, *Geophys. Res. Lett*, *36*, doi:10.1029/2009GL040303.

Day, S. M. (1982), Three-dimensional finite difference simulation of fault dynamics: rectangular faults with fixed rupture velocity, *Bull. Seismol. Soc. Am.*, *72*(3), 705–727.

Day, S. M., G. Yu, and D. J. Wald (1998), Dynamic stress changes during earthquake rupture, *Bull. Seismol. Soc. Am.*, *88*(2), 512–522.

Day, S. M., L. A. Dalguer, N. Lapusta, and Y. Liu (2005), Comparison of finite difference and boundary integral solutions to three-dimensional spontaneous rupture, *J. Geophys. Res.*, *110*, doi:10.1029/2005jb003813.

Denolle, M. A., and P. M. Shearer (2016), New perspectives on self-similarity for shallow thrust earthquakes, *J. Geophys. Res.*, *121*, 6533–6565, doi:10.1002/2016JB013105.

Dieterich, J. H. (1979), Modeling of rock friction: 1. experimental results and constitutive equations, *J. Geophys. Res.*, *84*(B5), 2161–2168, doi:10.1029/JB084iB05p02161.

Dunham, E. M., D. Belanger, L. Cong, and J. E. Kozdon (2011), Earthquake ruptures with strongly rate-weakening friction and off-fault plasticity, part 1: planar faults, *Bull. Seismol. Soc. Am.*, *101*(5), 2296–2307, doi:10.1785/0120100075.

Ely, G. P., S. M. Day, and J.-B. Minster (2008), A support-operator method for viscoelastic wave modelling in 3-D heterogeneous media, *Geophys. J. Int.*, *172*(1), 331–344, doi:10.1111/j.1365-246X.2007.03633.x.

Ely, G. P., S. M. Day, and J.-B. Minster (2009), A support-operator method for 3-D rupture dynamics, *Geophys. J. Int.*, *177*(3), 1140–1150, doi:10.1111/j.1365-246X.2009.04117.x.

Ely, G. P., S. M. Day, and J.-B. Minster (2010), Dynamic rupture models for the southern San Andreas fault, *Bull. Seismol. Soc. Am.*, *100*(1), 131–150, doi:10.1785/0120090187.

Eshelby, J. D. (1957), The determination of the elastic field of an ellipsoidal inclusion, and related problems, *Proc. R. Soc. A*, *241*(1226), 376–396, doi:10.1098/rspa.1957.0133.

Gabriel, A. A., J. P. Ampuero, L. A. Dalguer, and P. M. Mai (2012), The transition of dynamic rupture styles in elastic media under velocity-weakening friction, *J. Geophys. Res.*, *117*, doi:10.1029/2012JB009468.

Hanks, T. C., and R. K. McGuire (1981), The character of high-frequency strong ground motion, *Bull. Seismol. Soc. Am.*, *71*(6), 2071–2095.

Hanks, T. C., and W. Thatcher (1972), Graphical representation of seismic source parameters, *J. Geophys. Res.*, *77*(23), 4393–4405, doi:10.1029/JB077i023p04393.

Harris, R. A., M. Barall, R. Archuleta, E. Dunham, B. Aagaard, J. P. Ampuero, H. Bhat, V. Cruz-Atienza, L. Dalguer, P. Dawson, S. Day, B. Duan, G. Ely, Y. Kaneko, Y. Kase, N. Lapusta, Y. Liu, S. Ma, D. Oglesby, K. Olsen, A. Pitarka, S. Song, and E. Templeton (2009), The SCEC/USGS dynamic earthquake rupture code verification exercise, *Seismol. Res. Lett.*, *80*(1), 119–126.

Haskell, N. A. (1964), Total energy and energy spectral density of elastic wave radiation from propagating faults, *Bull. Seismol. Soc. Am.*, *54*(6A), 1811–1841.

Heaton, T. H. (1990), Evidence for and implications of self-healing pulses of slip in earthquake rupture, *Phys. Earth Planet. Int*, *64*(1), 1–20.

Hirano, S., and Y. Yagi (2017), Dependence of seismic and radiated energy on shorter wavelength components, *Geophys. J. Int.*, *209*(3), 1585–1592, doi:10.1093/gji/ggx108.

Huang, Y. H., and J. P. Ampuero (2011), Pulse-like ruptures induced by low-velocity fault zones, *J. Geophys. Res.*, *116*, doi:10.1029/2011JB008684.

Imanishi, K., and W. L. Ellsworth (2013), Source scaling relationships of microearthquakes at Parkfield, CA, Determined Using the SAFOD Pilot Hole Seismic Array, in *Earthquakes: Radiated Energy and the Physics of Faulting*, pp. 81–90, American Geophysical Union, doi:10.1029/170GM10.

Johnson, E. (1992), The influence of the lithospheric thickness on bilateral slip, *Geophys. J. Int.*, *108*(1), 151–160.

Kanamori, H., and D. L. Anderson (1975), Theoretical basis of some empirical relations in seismology, *Bull. Seismol. Soc. Am.*, *65*(5), 1073–1095.

Kanamori, H., and L. Rivera (2006), Energy partitioning during an earthquake, in *Earthquakes: Radiated Energy and the Physics of Faulting*, pp. 3–13, American Geophysical Union, doi:10.1029/170GM03.

Kaneko, Y., and P. M. Shearer (2014), Seismic source spectra and estimated stress drop derived from cohesive-zone models of circular subshear rupture, *Geophys. J. Int.*, *197*(2), 1002–1015, doi:10.1093/gji/ggu030.

Kaneko, Y., and P. M. Shearer (2015), Variability of seismic source spectra, estimated stress drop, and radiated energy, derived from cohesive-zone models of symmetrical and asymmetrical circular and elliptical ruptures, *J. Geophys. Res.*, *120*(2), 1053–1079, doi:10.1002/2014jb011642.

Lapusta, N., J. R. Rice, Y. Ben-Zion, and G. T. Zheng (2000), Elastodynamic analysis for slow tectonic loading with spontaneous rupture episodes on faults with rate- and state-dependent friction, *J. Geophys. Res.*, *105*(B10), 23,765–23,789, doi:10.1029/2000JB900250.

Leonard, M. (2010), Earthquake fault scaling: self-consistent relating of rupture length, width, average displacement, and moment release, *Bull. Seismol. Soc. Am.*, *100*(5A), 1971–1988, doi:10.1785/0120090189

Lu, X., N. Lapusta, and A. J. Rosakis (2010), Pulse-like and crack-like dynamic shear ruptures on frictional interfaces: experimental evidence, numerical modeling, and implications, *Int. J. Fract.*, *163*(1-2), 27–39.

Madariaga, R. (1976), Dynamics of an expanding circular fault, *Bull. Seismol. Soc. Am.*, *66*(3), 639–666.

Madariaga, R. (1977a), Implications of stress-drop models of earthquakes for inversion of stress drop from seismic observations, *Pure. Appl. Geophys.*, *115*(1-2), 301–316.

Madariaga, R. (1977b), High-frequency radiation from crack (stress drop) models of earthquake faulting, *Geophys. J. R. Astron. Soc.*, *51*(3), 625–651, doi:10.1111/j.1365-246X.1977.tb04211.x.

Marone, C. (1998), Laboratory-derived friction laws and their application to seismic faulting, *Annu. Rev. Earth Planet. Sc.*, *26*, 643–696.

Molnar, P., B. E. Tucker, and J. N. Brune (1973), Corner frequencies of P and S waves and models of earthquake sources, *Bull. Seismol. Soc. Am.*, *63*(6), 2091–2104.

Nielsen, S., and R. Madariaga (2003), On the self-healing fracture mode, *Bull. Seismol. Soc. Am.*, *93*(6), 2375–2388, doi:10.1785/0120020090.

Noda, H., E. M. Dunham, and J. R. Rice (2009), Earthquake ruptures with thermal weakening and the operation of major faults at low overall stress levels, *J. Geophys. Res.*, *114*, doi:10.1029/2008jb006143.

Noda, H., N. Lapusta, and H. Kanamori (2013), Comparison of average stress drop measures for ruptures with heterogeneous stress change and implications for earthquake physics, *Geophys. J. Int.*, *193*(3), 1691–1712.

Oglesby, D. D., and S. M. Day (2002), Stochastic fault stress: Implications for fault dynamics and ground motion, *Bull. Seismol. Soc. Am.*, *92*(8), 3006–3021.

Perrin, G., J. R. Rice, and G. Zheng (1995), Self-healing slip pulse on a frictional surface, *J. Mech. Phys. Solids*, *43*(9), 1461–1495.

Prejean, S. G., and W. L. Ellsworth (2001), Observations of earthquake source parameters at 2 km depth in the Long Valley Caldera, eastern California, *Bull. Seismol. Soc. Am.*, *91*(2), 165–177.

Prieto, G. A., P. M. Shearer, F. L. Vernon, and D. Kilb (2004), Earthquake source scaling and self-similarity estimation from stacking P and S spectra, *J. Geophys. Res.*, *109*, doi: 10.1029/2004jb003084.

Rojas, O., E. M. Dunham, S. M. Day, L. A. Dalguer, and J. E. Castillo (2009), Finite difference modelling of rupture propagation with strong velocity-weakening friction, *Geophys. J. Int.*, *179*(3), 1831–1858.

Rudnicki, J. W., and L. B. Freund (1981), On energy radiation from seismic sources, *Bull. Seismol. Soc. Am.*, *71*(3), 583–595.

Ruina, A. (1983), Slip instability and state variable friction laws, *J. Geophys. Res.*, *88*(B12), 10,359–10,370, doi:10.1029/JB088iB12p10359.

Sato, T., and T. Hirasawa (1973), Body wave spectra from propagating shear cracks, *J. Phys. Earth*, *21*(4), 415–431, doi:10.4294/jpe1952.21.415.

Savage, J. C. (1966), Radiation from a realistic model of faulting, *Bull. Seismol. Soc. Am.*, *56*(2), 577–592.

Savage, J. C. (1972), Relation of corner frequency to fault dimensions, *J. Geophys. Res.*, *77*(20), 3788–3795, doi:10.1029/JB077i020p03788.

Shao, G., C. Ji, and E. Hauksson (2012), Rupture process and energy budget of the 29 July 2008 Mw 5.4 Chino Hills, California, earthquake, *J. Geophys. Res.*, *117*, doi: 10.1029/2011JB008856.

Shaw, B. E. (2003), Magnitude dependence of radiated energy spectra: Far-field expressions of slip pulses in earthquake models, *J. Geophys. Res.*, *108*(B2), doi: doi:10.1029/2001JB000741.

Shearer, P. M., G. A. Prieto, and E. Hauksson (2006), Comprehensive analysis of earthquake source spectra in southern California, *J. Geophys. Res.*, *111*, doi: 10.1029/2005JB003979.

Shi, Z. Q., and S. M. Day (2013), Rupture dynamics and ground motion from 3-D rough-fault simulations, *J. Geophys. Res.*, *118*(3), 1122–1141, doi:10.1002/jgrb.50094.

Somerville, P., K. Irikura, R. Graves, S. Sawada, D. Wald, N. Abrahamson, Y. Iwasaki, T. Kagawa, N. Smith, and A. Kowada (1999), Characterizing crustal earthquake slip models for the prediction of strong ground motion, *Seismol. Res. Lett.*, *70*(1), 59–80.

Song, S. G. (2015), The effect of fracture energy on earthquake source correlation statistics, *Bull. Seismol. Soc. Am.*, *105*(2a), 1042–1048.

Song, S. G., L. A. Dalguer, and P. M. Mai (2013), Pseudo-dynamic source modelling with 1-point and 2-point statistics of earthquake source parameters, *Geophys. J. Int.*, *196*(3), 1770–1786.

Stork, A. L., and H. Ito (2004), Source parameter scaling for small earthquakes observed at the western Nagano 800-m-deep borehole, central japan, *Bull. Seismol. Soc. Am.*, *94*(5), 1781–1794.

Uchide, T., and K. Imanishi (2016), Small earthquakes deviate from the omega-square model as revealed by multiple spectral ratio analysis, *Bull. Seismol. Soc. Am.*, *106*(3), 1357–1363, doi:10.1785/0120150322.

Vyas, J. C., P. M. Mai, and M. Galis (2016), Distance and azimuthal dependence of ground-motion variability for unilateral strike-slip ruptures, *Bull. Seismol. Soc. Am.*, *106*(4), 1584–1599.

Zheng, G., and J. R. Rice (1998), Conditions under which velocity-weakening friction allows a self-healing versus a cracklike mode of rupture, *Bull. Seismol. Soc. Am.*, *88*(6), 1466–1483.